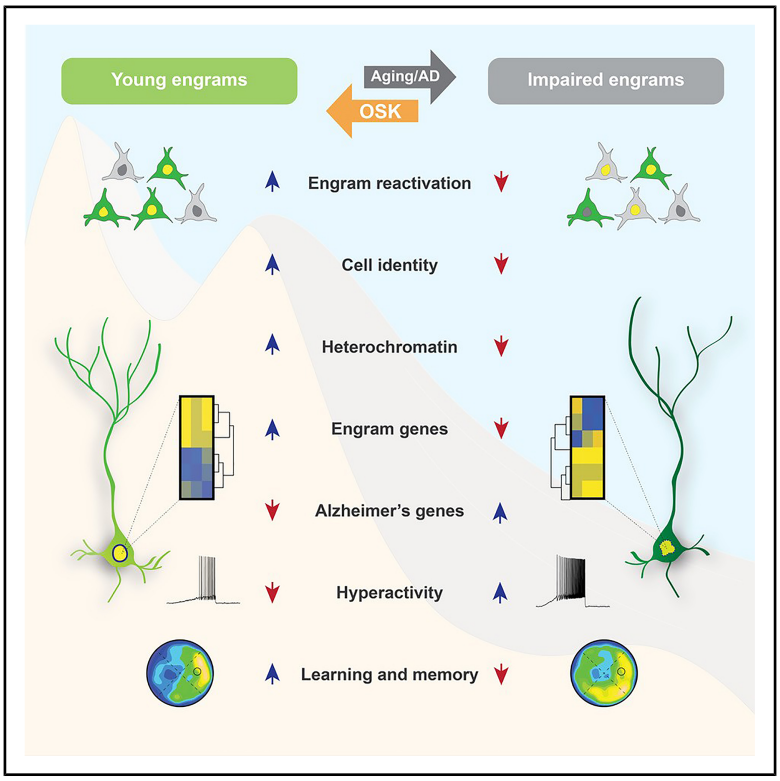
Neuron

Article

Cognitive rejuvenation through partial reprogramming of engram cells

Graphical abstract



Highlights

- Partial reprogramming of engram cells restores youthful markers in age and AD
- In AD mice, it rectifies epigenetic, transcriptional, and excitability aberrations
- Learning improvements across ages and disease suggest cognitive rejuvenation

Authors

Gabriel Berdugo-Vega, Cesar Sierra, Simone Astori, ..., Marianne Julie Scoglio, Carmen Sandi, Johannes Gräff

Correspondence

gabriel.berdugovega@epfl.ch (G.B.-V.), johannes.graeff@epfl.ch (J.G.)

In brief

Berdugo-Vega et al. combine partial reprogramming and engram technologies to achieve molecular rejuvenation of learning-associated neuronal ensembles. Engram reprogramming counteracts molecular, cellular, and electrophysiological signs of aging and disease and is associated with behavioral improvements that are consistent with a rejuvenation of learning and memory capacities.

Berdugo-Vega et al., 2026, Neuron *114*, 1–15
March 18, 2026 © 2025 The Author(s). Published by Elsevier Inc.
https://doi.org/10.1016/j.neuron.2025.11.028

CellPress

Please cite this article in press as: Berdugo-Vega et al., Cognitive rejuvenation through partial reprogramming of engram cells, Neuron (2025), https://doi.org/10.1016/j.neuron.2025.11.028

Neuron

CellPress
OPEN ACCESS

Article

Cognitive rejuvenation through partial reprogramming of engram cells

Gabriel Berdugo-Vega,[1,*] Cesar Sierra,[1] Simone Astori,[1,2] Veronika Calati,[1] Jules Orsat,[1] Marianne Julie Scoglio,[1] Carmen Sandi,[2,3] and Johannes Gräff[1,3,4,*]

[1]Laboratory of Neuroepigenetics, Brain Mind Institute, School of Life Sciences, École Polytechnique Fédérale Lausanne, 1015 Lausanne, Switzerland

[2]Laboratory of Behavioral Genetics, Brain Mind Institute, School of Life Sciences, École Polytechnique Fédérale de Lausanne, 1015 Lausanne, Switzerland

[3]Synapsy Center for Mental Health Research, School of Life Sciences, École Polytechnique Fédérale de Lausanne, 1015 Lausanne, Switzerland

[4]Lead contact

*Correspondence: gabriel.berdugovega@epfl.ch (G.B.-V.), johannes.graeff@epfl.ch (J.G.)

https://doi.org/10.1016/j.neuron.2025.11.028

SUMMARY

Counteracting cognitive decline is a declared goal of regenerative medicine. Recently, partial cellular reprogramming has emerged as a promising strategy to promote tissue regeneration and restore cellular function, but whether this approach bears fruit when targeted to cell populations underlying cognitive processes remains unknown. Here, we report that partial reprogramming of engram neurons—*bona fide* memory trace cells—by OSK-mediated gene therapy reversed the expression of senescence- and disease-related cellular hallmarks in aged mice and models of Alzheimer's disease (AD), re-established aberrant epigenetic-transcriptional patterns pertaining to synaptic plasticity, and counteracted AD-typical neuronal hyperexcitability. Importantly, irrespective of the brain area targeted or the behavioral paradigm employed, engram reprogramming also recovered learning and memory capacities to levels of healthy young animals, suggesting cognitive rejuvenation. These results posit that partial reprogramming of specific cell populations in the brain can be exploited for cognitive restoration in aging and disease.

INTRODUCTION

Partial cellular reprogramming has emerged as one of the most promising strategies in regenerative medicine. Cyclic expression of the four Yamanaka factors (Oct4, Sox2, Klf4, and cMyc—OSKM), or a partial combination thereof (OSK), holds the potential to orchestrate rejuvenation of cellular function in aging while at the same time preventing changes in cell identity and tumorigenesis.[1,2] Partial reprogramming has been used at the whole-body or entire tissue level in mice to successfully extend lifespan,[3,4] to promote regeneration of pancreatic, hepatic, and muscle tissue,[3,5,6] and to restore vision in models of blindness.[7,8] Recently, beneficial effects of partial reprogramming approaches, starting from a young age, have also been observed to preserve cognitive abilities during aging and disease,[9–13] but whether mnemonic functions can be rescued by partial reprogramming after the onset of cognitive decline remains unknown.

Memories are encoded in sparse neuronal ensembles termed engrams,[14,15] which are found in different brain regions, with specific contributions to recall during memory consolidation. Thus, engrams in the hippocampus, and in particular in the dentate gyrus (DG), are predominantly important for learning and recent recall,[16,17] whereas engrams in the medial prefrontal cortex (mPFC) become gradually more relevant for remote memory expression.[18,19] Importantly, during physiological aging and in mouse models of Alzheimer's disease (AD), engram impairments interfere with memory recall,[20–23] suggesting that engram dysfunction may underlie age- and disease-related memory decline. However, the molecular changes leading to engram malfunction in aging or AD have not been explored, and, consequently, sustained means to counteract these deficits and rescue memory remain to be identified.

RESULTS

Partial reprogramming of engram cells rescues age-related impairments in learning and memory

We first investigated the potential of partial cellular reprogramming of engram cells, defined as learning-activated c-Fos$^+$ ensembles, to ameliorate cognitive function during physiological aging. For this, we stereotaxically delivered adeno-associated viruses designed to label (c-Fos:ttA + TRE::GFP) and to partially reprogram (+TRE::OSK) engram cells responsible for learning in the hippocampal DG of aged mice (here defined as 9–10 months old) and, as controls, young wild-type (WT) mice (2–3 months old) (Figure 1A). With this tet-off system, engram identification

This is an open access article under the CC BY license (http://creativecommons.org/licenses/by/4.0/).

Please cite this article in press as: Berdugo-Vega et al., Cognitive rejuvenation through partial reprogramming of engram cells, Neuron (2025), https://doi.org/10.1016/j.neuron.2025.11.028

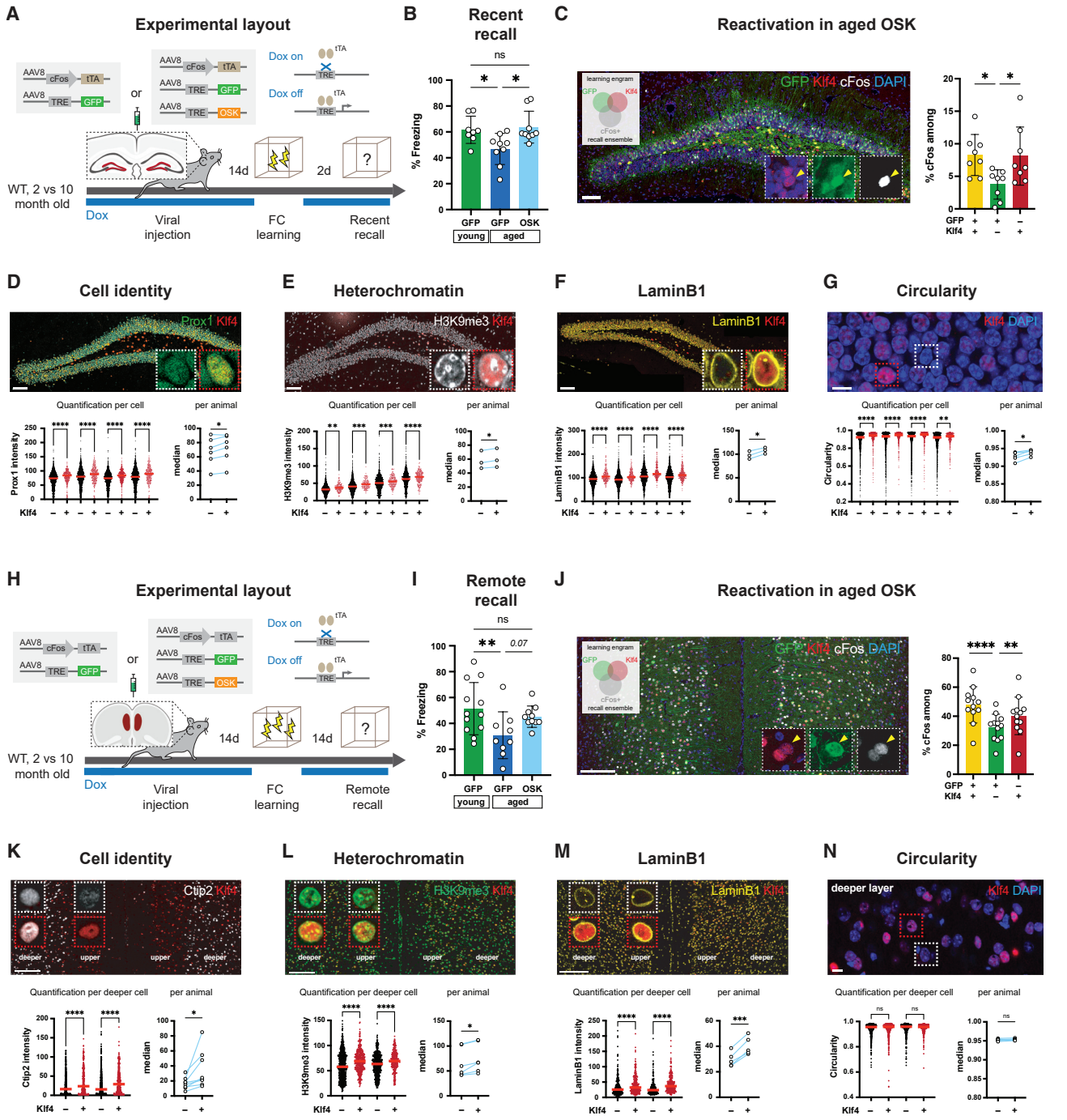


Figure 1. Partial reprogramming of engram cells rescues age-related cellular hallmarks and memory

(A) Scheme depicting the experimental design for engram reprogramming during physiological aging, including the viral constructs used for DG engram targeting, functioning of the tet-off conditional expression system, and behavioral protocol. Note that conditional transgene expression was directed exclusively to engram cells activated by learning (c-Fos$^+$) through removal and re-introduction of Dox around the fear conditioning experience.

(B) Percentage of freezing at recent recall (2 days after conditioning) of young (dark green) and aged mice injected with GFP (dark blue) and OSK (light blue), showing decreased freezing in GFP-injected aged mice and recovery upon OSK expression.

(C) Immunofluorescence picture with magnifications and quantification for reactivation (c-Fos$^+$) in OSK-injected aged mice of non-reprogrammed (GFP$^+$Klf4$^-$) vs. reprogrammed (GFP$^-$Klf4$^+$ and GFP$^+$Klf4$^+$, yellow arrowhead) DG engrams.

(D–G) Immunofluorescence picture with magnifications (top; representative Klf4$^-$ and Klf4$^+$ in white and red insets, respectively) and quantifications (bottom) of cell identity (Prox1, D) and age-related markers (H3K9me3, E; LaminB1, F; circularity, G) of OSK-injected aged mice. Intensity data are shown as raw values per

(legend continued on next page)

Please cite this article in press as: Berdugo-Vega et al., Cognitive rejuvenation through partial reprogramming of engram cells, Neuron (2025), https://doi.org/10.1016/j.neuron.2025.11.028

and the induction of the reprogramming factors can be temporally controlled by doxycycline (Dox) withdrawal from the drinking water, which triggers the expression of the tetracycline-responsive element (TRE), driving GFP and OSK. We synchronized Dox withdrawal to the learning phase of a contextual fear conditioning paradigm, an associative memory task, after which animals were immediately re-introduced on Dox. RNAscope analysis in animals sacrificed 90 min after learning confirmed simultaneous OSK expression in DG-activated ensembles (Figures S1A–S1E), as well as their downregulation to background expression levels after Dox re-introduction (Figures S1F–S1H).

We assessed the effect of OSK-mediated reprogramming on memory with a recall test 2 days after learning, a time at which reprogrammed and non-reprogrammed engrams can be identified by Klf4 and GFP protein immunoreactivity, respectively (Figures S1I, S1J, and S2A). We found that aged control mice injected with GFP showed decreased freezing compared with young mice (Figure 1B), indicative of age-related impairments in fear memory. This behavioral phenotype was associated with decreased engram reactivation in the DG (Figure S2B), in line with previous reports.[23] In contrast, memory in OSK-injected aged animals was rescued to that of young mice (Figure 1B). Furthermore, we observed that reprogrammed Klf4$^+$ engrams were preferentially reactivated over non-reprogrammed engrams (Figure 1C), indicating that engram-specific overexpression of OSK can rescue against age-related deficits in associative memory.

Next, we studied the effect of OSK induction on several age-related cellular markers. First, we quantified the levels of Prox1, a cell-type-specific identity determinant for DG granule neurons,[24] in Klf4$^+$ and Klf4$^-$ cells in order to exclude that partial cellular reprogramming would lead to cellular de-differentiation. Instead, we found that partial reprogramming consistently increased expression levels of Prox1 compared with non-reprogrammed cells (Figure 1D) as well as with non-reprogrammed engrams (Figure S2C). This was due to a decrease in the proportion of low-expressing Prox1$^+$ cells among the Klf4$^+$ population (Figure S2D, left), thereby ameliorating deficits in Prox1 expression observed in engrams of aged GFP-injected animals (Figure S2D, right). These results suggest that OSK induction does not lead to a loss in cell identity but rather strengthens it. Subsequently, we examined the expression of H3K9me3, LaminB1, and nuclear circularity, which are markers related to heterochromatin and the nuclear architecture known to decrease during aging.[25–29] We observed increased expression of H3K9me3 (Figure 1E) and LaminB1 (Figure 1F), as well as increased nuclear circularity (Figure 1G), in reprogrammed engram cells (Figure S2E). Together, these results indicate that OSK-mediated partial engram reprogramming counteracts the expression of age-related parameters without leading to a loss in cellular identity.

We then sought to assess the potential of OSK to also rescue more durable, so-called remote, forms of memory. For this, we targeted engrams in the mPFC, which have been shown to be relevant for remote memory recall (i.e., 2 weeks after learning).[18,19] Cortical engrams of young and aged mice were tagged and reprogrammed during fear conditioning as before (Figure 1H). RNAscope analysis confirmed OSK expression in learning engrams as well as downregulation to background levels after Dox re-introduction (Figures S3A–S3H). When tested for remote memory retention 2 weeks later, we found that while GFP-injected aged mice showed a decrease in freezing, indicating remote memory impairment, OSK-injected aged animals no longer displayed such impairment (Figure 1I). Furthermore, reprogrammed engrams in the mPFC, identified by Klf4 immunoreactivity (Figures S3I, S3J, and S4A), showed increased reactivation upon recall (Figure 1J).

At the cellular level, we noticed that OSK-expressing viruses predominantly infected engram cells in deeper layers of the mPFC (Figure S4B). Consequently, we quantified the levels of Ctip2, a marker of deeper layer neurons, and found its expression to be enhanced upon partial reprogramming (Figures 1K and S4C). Additionally, we observed that OSK infection led to an increase in H3K9me3 and LaminB1 (Figures 1L and 1M) and a reduced percentage of low-circularity neurons in deeper layers (Figures 1N and S4C). Taken together, these results suggest that partial cellular reprogramming also promotes cortical engram functions in the aged brain, without leading to a loss in cell identity, and improves the retention of remote memories.

Partial reprogramming of engram cells rescues spatial learning and memory deficits in AD

We next investigated whether partial engram reprogramming would also be beneficial in the context of age-related neurodegenerative disorders, such as AD. For this, we used APP/PS1

cell, with intra-section comparisons between Klf4$^-$ (black) and Klf4$^+$ (red) of one example animal (left), as well as median value of Klf4$^-$ and Klf4$^+$ cells per animal (right).

(H) Scheme and experimental design for mPFC engram targeting.

(I) Percentage of freezing at remote recall (2 weeks after conditioning) of young and aged mice injected with GFP and OSK, as indicated, showing decreased freezing in GFP-injected aged mice and recovery upon OSK expression.

(J) Immunofluorescence with magnifications and quantification for reactivation (c-Fos$^+$) in OSK-injected aged mice of non-reprogrammed (GFP$^+$Klf4$^-$) vs. reprogrammed (GFP$^-$Klf4$^+$ and GFP$^+$Klf4$^+$, yellow arrowhead) mPFC engrams.

(K–N) Immunofluorescence with magnifications (top; representative Klf4$^-$ and Klf4$^+$ in white and red insets, respectively) and quantifications (bottom) of cell identity (Ctip2, K) and age-related markers (H3K9me3, L; LaminB1, M; circularity, N) of OSK-injected aged mice. Intensity data are shown as per cell, with intra-section comparisons between Klf4$^-$ (black) and Klf4$^+$ (red) of one example section (left), as well as median value of Klf4$^-$ and Klf4$^+$ cells per animal (right) in deeper layers. Scale bars: 100 (C–F), 200 (J–M), or 10 (G and N) μm. Data are represented as bar graphs, with individual animal values (dots; $N \geq 8$ male WT mice for behavior and reactivation), median intensity value in arbitrary units per animal ($N \geq 3$), or as individual cells ($n > 300$) with median (red line). Error bars indicate SD. ****$p < 0.0001$; ***$p < 0.001$; **$p < 0.01$; *$p < 0.05$; ns, non-significant, by tests as indicated in Table S7.

See also Figures S1–S4.

Please cite this article in press as: Berdugo-Vega et al., Cognitive rejuvenation through partial reprogramming of engram cells, Neuron (2025), https://doi.org/10.1016/j.neuron.2025.11.028

mice, an extensively used model of AD that expresses human mutations for the *App* and *Psen1* genes (coding for the amyloid-β precursor and presenilin 1 proteins, respectively) and that is characterized by early plaque deposition and cognitive impairments from middle age onward.[30] Using the same experimental setup as before, we observed increased expression of the cell identity markers Prox1 and Ctip2 in DG and mPFC engrams of aged APP/PS1 mice upon partial engram reprogramming (Figure S5A), as well as an increased expression of LaminB1 in both brain areas (Figure S5B), which is known to be downregulated in APP/PS1 mice.[31] These findings extend the previously observed beneficial effects of partial engram reprogramming at the cellular level from aging to an AD context.

Consequently, we tested whether engram reprogramming would also rescue learning and memory in APP/PS1 mice. Because this mouse strain does not show impairments in fear memory (Figure S5C),[32] we employed a water maze navigational paradigm, a method of choice when assessing memory loss in mouse models of AD,[33,34] with the added benefit of being able to reveal changes in learning strategies. We first performed DG reprogramming experiments, in which the labeling window for the tagging of putative engram cells was opened at the beginning of a 5-day-long water maze training protocol, designed to allow for transgene expression and evaluate differences during learning (Figure 2A). As mice learn to locate the hidden position of the submerged platform, they normally progress from the use of random and non-spatial strategies to more efficient and spatially directed ones that depend on hippocampal functioning (Figure 2B).[35,36] We observed that GFP-injected APP/PS1 mice showed reduced use of hippocampal strategies and longer path lengths relative to GFP-injected WT controls (Figures 2C and 2D), indicative of impaired navigation. In contrast, OSK-injected APP/PS1 mice no longer displayed this impairment and showed a significantly increased contribution of hippocampal strategies throughout the learning phase (Figures 2C and 2D), suggesting that spatial learning in APP/PS1 mice can be improved upon DG engram reprogramming.

Subsequently, we investigated whether partial engram reprogramming could also recover spatial memories. For this, we injected OSK into the mPFC of APP/PS1 mice and used a shorter and more exhaustive, 3-day-long water maze learning paradigm, in which the engram-labeling window was targeted to the last learning day (Figure 2E; see STAR Methods). In this paradigm, GFP-injected APP/PS1 mice also showed reduced use of hippocampal learning (Figure 2F), which resulted in an absence of spatial memory as assessed by target quadrant preference in a probe test at recent and remote times (Figures 2G and 2H). Conversely, we found that OSK-injected APP/PS1 mice, which also showed impaired learning and recent memory (Figures 2F and 2G), displayed a significant preference for the target quadrant that was comparable to that of WT mice when tested 2 weeks after learning (Figure 2H), indicating restored spatial memory. Importantly, targeting OSK expression to cells active during exploration of a novel environment prior to the water maze training did not result in spatial memory restoration, suggesting that the effects of engram reprogramming are memory specific (Figure S5D). Altogether, these results show that engram reprogramming in APP/PS1 mice can recover both spatial learning and memory retention.

Partial reprogramming of engram cells rescues molecular signatures of AD

To better understand the molecular mechanisms mediating the OSK-induced improvements in engram cells, we next assessed gene expression and chromatin accessibility changes by single-nucleus (sn) multiome sequencing (consisting of RNA sequencing [snRNA-seq] and assay for transposase-accessible chromatin sequencing [snATAC-seq]). To that end, we isolated mPFC nuclei of GFP-injected WT and APP/PS1 mice, as well as OSK-injected APP/PS1 mice, 1 day after the last recall session of the water maze paradigm (Figure 3A). After quality control (Figures S6A and S6B), all expected neuronal and glial subtypes of the mPFC were retrieved in proportions similar to those previously described (Figures 3B, S6C, and S6D).[37,38] In order to identify engram cells, we mapped RNA reads to the sequence of the viral vectors and detected them mostly among excitatory neurons (Figures 3C and S6E). Thus, in the following, we focused our analysis on excitatory engrams, henceforth referred to as WT, APP/PS1, or OSK (for other cell types; see Figure S6F and Table S1).

First, we analyzed transcriptional changes pertaining to cellular identity, engram formation, and AD pathology (see STAR Methods and Table S2). Supporting the notion that AD results in progressive cell de-differentiation,[39–41] we found that APP/PS1 engrams showed decreased expression of identity genes, which was fully rescued upon partial reprogramming (Figures 3D, left, and S6G). Next, we used genes differentially expressed either between engram and non-engram cells in WT animals or, alternatively, between WT and APP/PS1 engrams (referred to as WT and AD engram signatures, respectively; see Table S2), to score cells in pseudotime trajectories. In line with the presence of functional impairments in AD engram cells,[20] we found that APP/PS1 engrams showed a reduced engram score, which, upon OSK treatment, was partially restored (Figure 3D, center). A similar restoration by OSK was also observed for the AD engram score (Figure 3D, right), albeit in a different direction. These results suggest that OSK-mediated reprogramming rescues, at least in part, transcriptional impairments of engram cells in APP/PS1 mice.

From a gene ontology perspective, the AD engram signature was enriched in terms pertaining to synaptic and neuronal function, compared with those found in the overall APP/PS1 excitatory population (Figure S6H), and was largely reversed in OSK engrams (Figure S6I; Table S3). This restoration was also confirmed by gene set enrichment analysis (GSEA), with the majority of the signatures affected in APP/PS1 being reversed in OSK, which included cell-death, immune, translation, and synaptic pathways (Figures 3E and S6J; Table S4).

At the level of individual differentially expressed genes (DEGs), a significant fraction of both down- and upregulated DEGs in APP/PS1 were rescued upon OSK treatment (Figures 3F and 3G). These OSK-rescued genes belonged to the categories of synapse organization and potassium ion transport for the aberrantly downregulated genes in APP/PS1, including several voltage-gated ion channels and neuregulin 1

Please cite this article in press as: Berdugo-Vega et al., Cognitive rejuvenation through partial reprogramming of engram cells, Neuron (2025), https://doi.org/10.1016/j.neuron.2025.11.028

CellPress
OPEN ACCESS

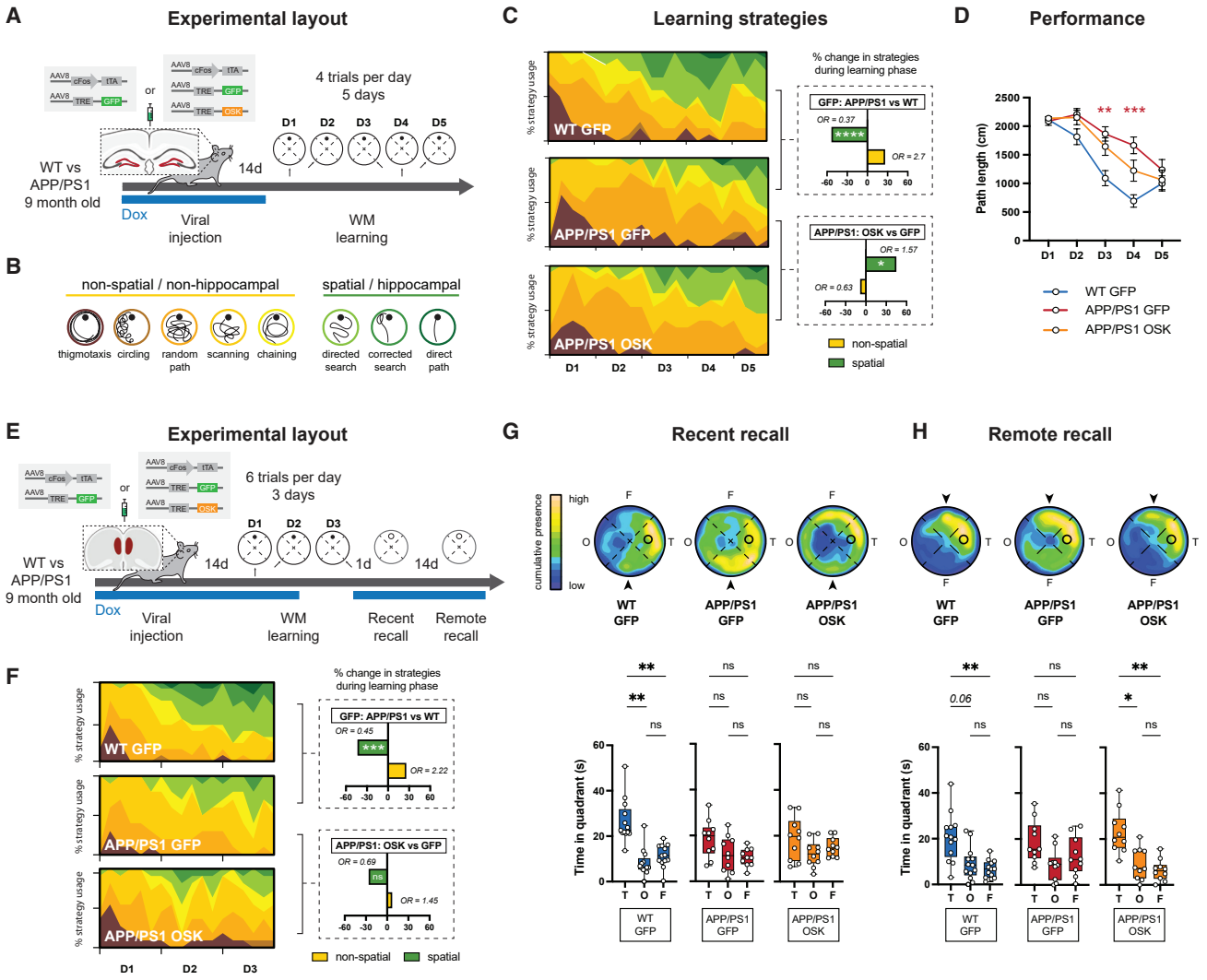


Figure 2. Partial reprogramming of engram cells rescues AD-related impairments in spatial memory

(A) Scheme depicting the experimental design for DG engram reprogramming in the context of AD. The labeling window opened from the start of a water maze navigational protocol, consisting on 5 days of spatial learning, 4 trials per day, with different starting positions each day.

(B and C) Drawings exemplifying color-coded searching trajectories, including non-spatial and spatial (i.e., hippocampal) strategies (B), and their mean contribution during the learning phase in WT and APP/PS1 mice injected with GFP or OSK, as indicated (C). Changes with odds ratios (ORs) in grouped spatial (green) and non-spatial (yellow) learning strategies are depicted and compared in GFP-injected APP/PS1 vs. WT (top) mice, as well as in OSK- vs. GFP-injected APP/PS1 (bottom) mice.

(D) Evolution of path length (cm) of GFP-injected WT (blue), GFP-injected APP/PS1 (red), and OSK-injected APP/PS1 (orange) mice throughout the 5 learning days. Note the significant increase in distance of GFP-injected APP/PS1 vs. WT mice on days 3 and 4 (in red), correlating with reduced use of spatial strategies (in C), and partial rescue upon OSK induction in DG engrams. $N = 14$ (WT GFP), 11 (APP/PS1 GFP), and 13 (APP/PS1 OSK) female mice.

(E) Experimental design for mPFC engram reprogramming in AD. The labeling window opened at the end of a shorter water maze protocol (3 days of spatial learning, 6 trials per day) with re-introduction of Dox after learning and including recent and remote memory recall.

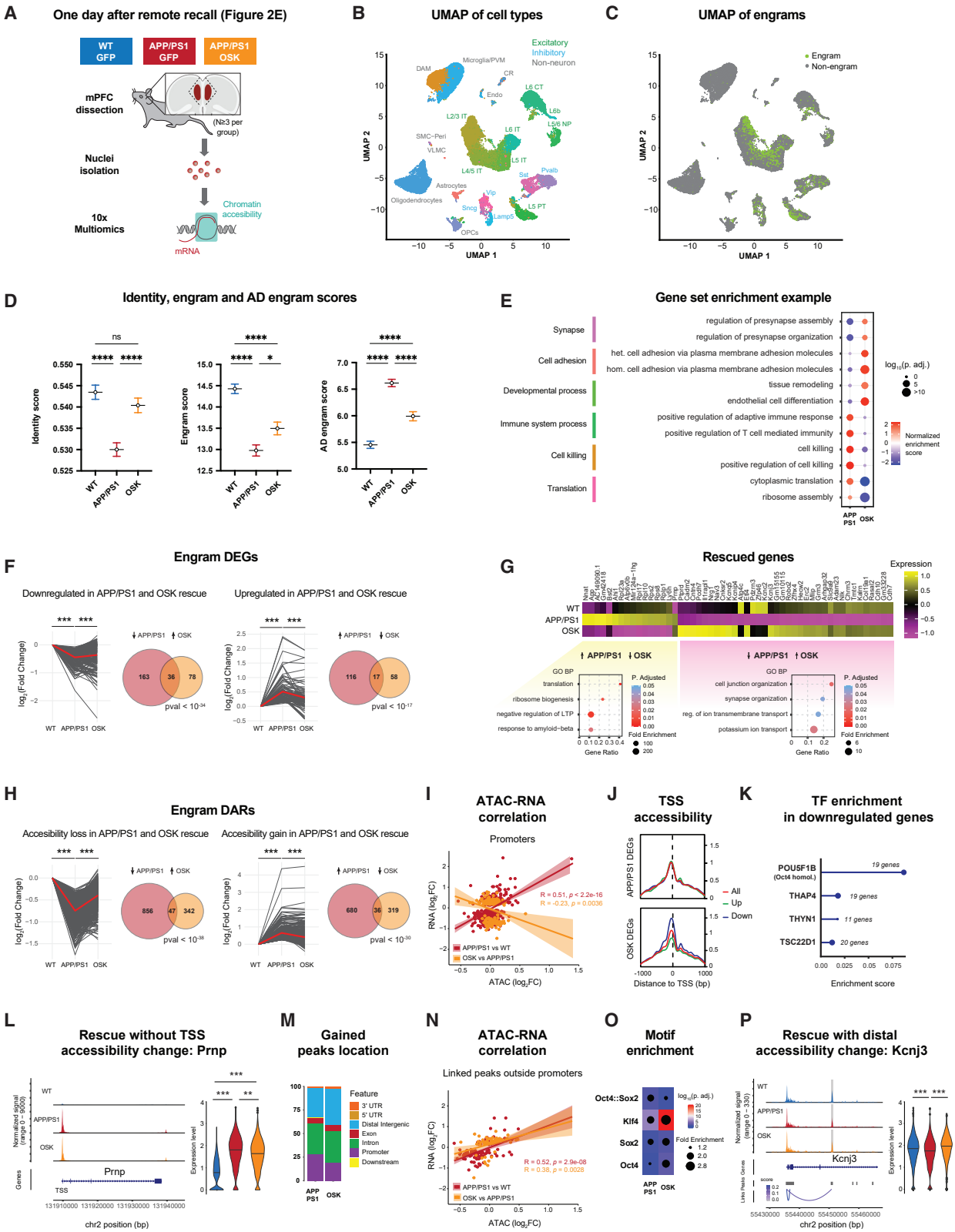
(F) Contribution and changes of spatial learning strategies between groups, showing impaired spatial navigation in APP/PS1 mice.

(G and H) Heatmaps (top) and quantifications (bottom) displaying quadrant preference (T, target; O, opposite; F, front) during the probe test at recent (G) and remote (H) times. Note the lack of preference for the target quadrant of all APP/PS1 mice at recent time and specific recovery of OSK-injected mice to WT levels at remote time. $N = 13$ (WT GFP) and 10 (APP/PS1, GFP and OSK) female mice. Data are represented as means ± SEM of each day (D) and as box-whisker plots with individual animals (G and H). ****$p < 0.0001$; ***$p < 0.001$; **$p < 0.01$; *$p < 0.05$; ns, non-significant, by tests as indicated in Table S7.

See also Figure S5.

(*Nrg1*),[42–44] and to amyloid beta response and negative regulation of long-term potentiation for the aberrantly upregulated genes in APP/PS1, encompassing key markers of AD neuropathology such as *App* and prion protein (*Prnp*)[45] (Figure 3G). Altogether, these findings suggest the presence of multifaceted deviations in the transcriptional landscape of APP/PS1 engrams, which were corrected upon partial reprogramming (Figure S7; Data S1).

Please cite this article in press as: Berdugo-Vega et al., Cognitive rejuvenation through partial reprogramming of engram cells, Neuron (2025), https://doi.org/10.1016/j.neuron.2025.11.028



(legend on next page)

Please cite this article in press as: Berdugo-Vega et al., Cognitive rejuvenation through partial reprogramming of engram cells, Neuron (2025), https://doi.org/10.1016/j.neuron.2025.11.028

Then, to explore changes in chromatin accessibility, we performed a differential accessibility analysis of all major cell types (Figures S8A–S8C; Table S5) and observed that a significant proportion of the differentially accessible regions (DARs) in APP/PS1 engram cells were reversed by OSK (Figure 3H). In order to elucidate whether and how these changes might mediate the DEGs, we analyzed the correlation between ATAC and RNA signals. Focusing first on promoters, we found that although transcriptional start site (TSS) accessibility positively correlated with gene expression changes in APP/PS1 engram cells (Figure 3I, red), this was not the case in OSK engrams (Figure 3I, orange), indicating a decoupling of chromatin openness with transcriptional activity. Moreover, we noticed that genes downregulated upon OSK had a more accessible TSS (Figure 3J), suggesting that OSK might repress gene expression through the recruitment of transcriptional regulators to open chromatin. Accordingly, when we used transcription factor enrichment analysis (ChEA3[46]) to identify factors associated with downregulated genes upon OSK, we found as the top candidate a homolog of Oct4 (*Pou5f1b*), alongside several other transcriptional regulators (Figure 3K; Table S6). One example of an OSK-rescued gene without accessibility changes at its TSS and associated with *Pou5f1b* was *Prnp* (Figure 3L). This mechanism is in line with previous reports showing that Oct4 can bind to open chromatin and promote the recruitment of transcriptional co-repressors.[47–49]

Expanding the analysis beyond promoters, we observed that the majority of OSK-induced gained peaks occurred in regions further away from the TSS (Figures 3M and S8D), which is in line with the reported binding of OSK factors to distal elements during full reprogramming.[50] Thus, we re-analyzed the correlation between ATAC and RNA changes, focusing exclusively on peaks defined as linked to the DEGs (see STAR Methods) but located outside of the promoters. This analysis yielded a positive correlation between accessibility and transcription in OSK engrams (Figure 3N, orange), which implies that OSK-mediated changes in gene expression also occur via accessibility gains in distal regions. Interestingly, these gained accessibility peaks were particularly enriched for Klf4 (Figure 3O), suggesting that this factor could act as the main mediator behind these changes (see also Figures S8E–S8G). One example of an OSK-rescued distal peak containing the Klf4 motif with concomitant increased gene expression concerned *Kcnj3* (Figure 3P). This gene codes for the potassium inwardly rectifying channel Kir3.1, which is important for maintaining membrane excitability[51] and has previously been linked to synaptic plasticity and memory[52,53] as well as AD.[54,55] Taken together, these results show that OSK mediates chromatin accessibility changes differently at proximal and distal genetic regions, with both contributing to the potential rescue of transcriptional aberrations in engram cells.

Partial reprogramming counteracts hyperexcitability in AD engram cells

Beyond these OSK-induced epigenetic-transcriptional changes in AD engrams, we asked whether their electrophysiological properties might also be altered. Intrinsic excitability (IE) is a central neuronal property for engram physiology during memory formation and recall,[56–59] known to be aberrantly increased in AD pyramidal neurons.[60–63] We therefore examined whether AD engram cells exhibit increased IE and the extent to which OSK-induced reprogramming could counteract these alterations, namely by performing *ex vivo* patch-clamp recordings

Figure 3. Partial reprogramming of engram cells rescues molecular signatures of AD

(A) Scheme depicting the experimental design for single-nucleus multiome assessment of mPFC engram reprogramming, including dissected mPFC of GFP-injected WT ($N = 3$), APP/PS1 ($N = 3$), and OSK-injected APP/PS1 ($N = 4$) female mice.

(B and C) Uniform manifold approximation and projection (UMAP) representing clusters of mPFC cell types extracted after quality control (B) and engrams within those (C).

(D) Quantification of cell identity, engram, and AD engram scores (see STAR Methods) in WT (blue), APP/PS1 (red), and OSK (orange) engrams (average per group with SEM; $n > 1,213$ engrams).

(E) GSEA depicting rescued transcriptional changes and related ontologies between APP/PS1 (APP/PS1 vs. WT) and OSK (OSK vs. APP/PS1) engrams (color coded as in Figure S6J).

(F and G) Analysis of DEGs in APP/PS1 engrams and their rescue upon OSK induction. Line-plot graphs represent genes with significantly changed expression in APP/PS1 relative to WT engrams and the corresponding change of the same genes in OSK engrams. Venn diagrams represent the intersection between significant DEGs of APP/PS1 (red) and OSK (orange) engrams (F). (G) Heatmaps of rescued genes in the three groups, with gene ontologies at the bottom.

(H) Analysis of DARs in APP/PS1 engrams and their rescue upon OSK induction, with line-plots and Venn diagrams as in (F).

(I) Correlation between RNA (DEGs) and ATAC (peaks in promoters) signals, in APP/PS1 (red) and OSK (orange) engrams.

(J) Chromatin accessibility in WT for DEGs found in APP/PS1 (top) and in APP/PS1 for DEGs found in OSK (bottom) engrams, with signal centered around the TSS.

(K) Top four ChEA3-extracted transcription factors expressed in engram cells and enriched among downregulated genes in OSK, with number of associated genes and ChEA3 score.

(L) Gene track of *Prnp*, as an example of an OSK-mediated rescued gene without changes in promoter accessibility, including peak signal and levels of gene expression in WT (blue), APP/PS1 (red), and OSK (orange) engrams.

(M) Genomic locations of gained peaks in APP/PS1 and OSK engrams, color coded as indicated.

(N) Correlation between RNA (DEGs) and ATAC (linked peaks located outside of promoters) signals, of groups as in (I).

(O) Heatmap of OSK factors' motif enrichment among gained peaks in APP/PS1 and OSK engrams.

(P) Gene track of *Kcnj3*, as an example of an OSK-mediated rescued gene with accessibility changes outside the TSS, including the location of its linked peak containing the Klf4 motif (gray area) and levels of gene expression in WT (blue), APP/PS1 (red), and OSK (orange) engrams. Data are shown with significance and fold enrichment as indicated. $^{****}p < 0.0001$; $^{***}p < 0.001$; $^{**}p < 0.01$; $^{*}p < 0.05$; ns, non-significant, by tests indicated in the STAR Methods section. CT, corticothalamic; CR, Cajal-Retzius; DAM, disease-associated microglia; Endo, endothelial cells; IT, intratelencephalic; L, layer; NP, near projecting; OPCs, oligodendrocyte precursors; PT, pyramidal tract; Pvalb, parvalbumin; PVM, perivascular macrophage; SMC-Peri, smooth muscle cells—pericytes; Sst, somatostatin; VLMC, vascular and leptomeningeal cell.

See also Figures S6–S8.

Please cite this article in press as: Berdugo-Vega et al., Cognitive rejuvenation through partial reprogramming of engram cells, Neuron (2025), https://doi.org/10.1016/j.neuron.2025.11.028

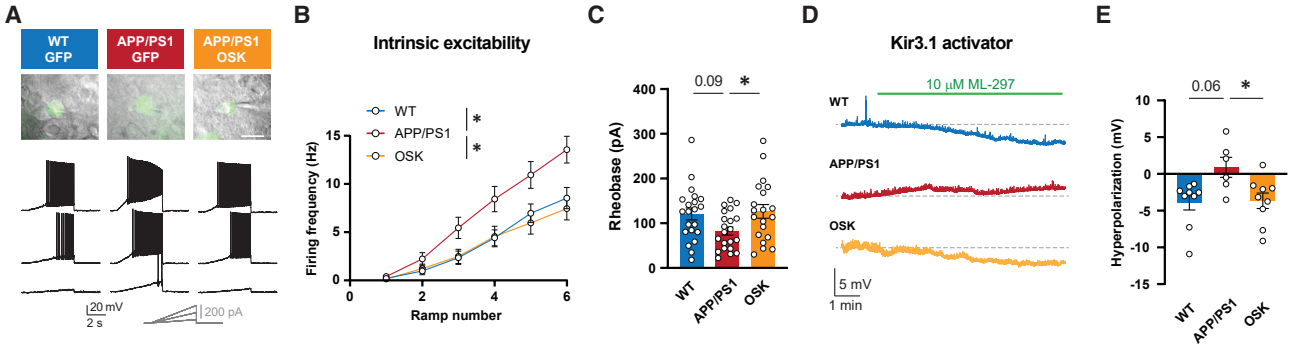


Figure 4. Partial reprogramming of engram cells rescues AD-related hyperexcitability

(A) Representative merged infrared and fluorescent images of GFP$^+$ pyramidal neurons patched in the prelimbic region of the mPFC from GFP-injected WT, APP/PS1, and OSK-injected APP/PS1 mice (top, $N = 5$ female mice per group), with example voltage traces showing action potential firing in response to somatic depolarization via ramped current injections (bottom).

(B and C) Mean firing frequency elicited by increasing depolarizations in WT (blue), APP/PS1 (red), and OSK (orange, identified as Klf4$^+$) engrams (B) and rheobase values (C), indicating hyperexcitability in APP/PS1 and normalized response in OSK engrams.

(D and E) Example voltage recordings showing the change in membrane potential upon perfusion of the Kir3.1 channel activator ML-297 (D) and mean values of ML-297-induced hyperpolarization (E). Note the restored membrane hyperpolarization in OSK engrams. Data are represented as mean per group (B; $n = 21$ for WT and APP/PS1 and 20 for OSK engrams) and bar graphs with individual dots indicating patched cells (C and E; $n > 5$). Scale bar: 20 μm. Error bars indicate SEM.

*$p < 0.05$, by tests as indicated in Table S7.

See also Figure S9.

in mPFC pyramidal engram cells (i.e., GFP$^+$ neurons) from WT, APP/PS1, and OSK mice. We found that APP/PS1 engram cells displayed hyperexcitability, consistent with previous observations in non-engram pyramidal neurons.[60,61] Specifically, APP/PS1 engram cells fired significantly more action potentials in response to depolarizing current injections (Figures 4A and 4B), which was accompanied by a reduced rheobase (Figure 4C) compared with WT engrams. Passive membrane properties were comparable between conditions, although APP/PS1 engrams exhibited a more hyperpolarized resting membrane potential (Figure S9A). Notably, OSK treatment rescued IE by normalizing firing frequencies (Figure 4B) and rheobase (Figure 4C) of APP/PS1 neurons toward WT levels. This normalization was also observed when comparing Klf4$^+$ and Klf4$^-$ engram cells within the same OSK-injected animals (Figures S9B–S9D), suggesting that IE was rescued specifically in reprogrammed engram cells.

Next, guided by the results from our multiome analysis (Figure 3P), we specifically investigated the role of Kir3.1 (coded by the *Kcnj3* gene) as a potential mediator of the observed electrophysiological changes. For this, we evaluated the effect of the Kir3.1 channel activator ML-297[54,64] on membrane potential (Figure 4D). We found that although ML-297 reliably hyperpolarized WT engrams, it failed to do so in APP/PS1 engram cells (Figure 4E), consistent with *Kcnj3* downregulation driving hyperexcitability.[64] By contrast, OSK-reprogrammed engrams exhibited restored hyperpolarization following ML-297 application (Figure 4E), underscoring the OSK-rescued expression of *Kcnj3* as a contributing factor in the normalization of IE in AD engrams. These results exemplify how OSK-mediated restoration of molecular aberrations translates into neurophysiological properties important for engram function in AD neurons.

Partial reprogramming of engram cells leads to cognitive rejuvenation across ages and disease

Finally, we wondered whether the behavioral changes observed upon engram reprogramming during physiological aging (Figure 1) and in AD (Figure 2) reflect a more generalizable, and thus quantifiable, restoration of learning patterns toward those of younger mice. For this, we first assessed whether the animals' chronological age could be predicted from behavioral performance alone and, if so, whether the learning patterns of reprogrammed mice are reflective of a younger predicted age. Thus, we generated a regression model that maximized the correlation between chronological age and different spatial learning metrics (Figure 5A; see STAR Methods), which provided a multiparametric dataset richer than quadrant occupancy or freezing levels alone. We used four different age groups of GFP-injected WT mice, ranging from 16 to 90 weeks of age ($N = 39$ mice), which were trained in the same water maze protocol used in DG engram reprogramming experiments (Figure 2A). The resulting model, which we termed "cognitive clock," had a correlation of $R = 0.57$ ($p < 0.001$) and predicted age accurately with a median error of 10 weeks (Figures S10A and S10B), suggesting that chronological age can be inferred from spatial learning patterns. Then, to test whether engram reprogramming would lead to a deceleration of the cognitive clock, we used behavioral data from OSK-injected WT mice spanning a wide age range (either 40 or 90 weeks old, $N = 15$ and 7, respectively), which showed spatial learning and memory improvements compared with their GFP-injected counterparts (Figures S10C and S10D). We found that OSK-injected mice showed a significant reduction in predicted vs. chronological age (Figure 5B), in particular for the mice of advanced age, indicating that the cognitive clock accurately reflected the memory improvements upon engram reprogramming in aged mice.

Please cite this article in press as: Berdugo-Vega et al., Cognitive rejuvenation through partial reprogramming of engram cells, Neuron (2025), https://doi.org/10.1016/j.neuron.2025.11.028

CellPress
OPEN ACCESS

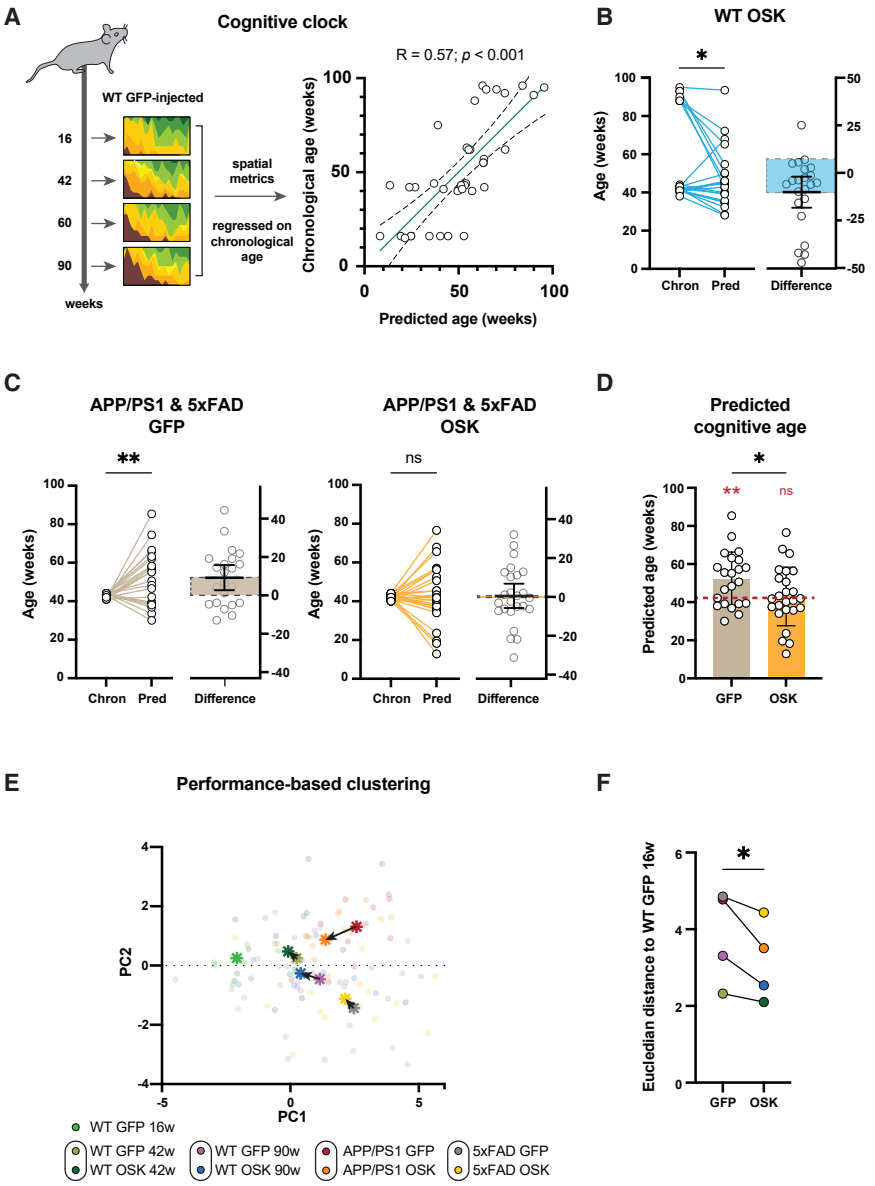


Figure 5. Partial engram reprogramming leads to cognitive rejuvenation across ages and disease

(A) Scheme depicting the experimental design for the generation of the cognitive clock. GFP-injected WT female mice of 16, 42, 60, and 90 weeks of age were tested in the same water maze paradigm as for DG engram reprogramming experiments (Figure 2A), and spatial learning metrics were regressed to their chronological age (in weeks) using an ordinary least-squares model adjusted for multicollinearity (see STAR Methods).

(B) Comparison of chronological and predicted ages of OSK-injected WT female mice (aged and old, on average 42 and 90 weeks old, respectively), showing a significant decrease in predicted age (left) and the magnitude of the difference (shaded area, right).

(C) Intra-group comparison of chronological and predicted ages, with estimation plots, of GFP-injected (left, in brown) and OSK-injected (right, in orange) AD (APP/PS1 female and 5xFAD male) mice.

(D) Inter-group comparison between predicted ages of GFP- (brown) and OSK-injected (orange) 42-week-old AD mice, showing restoration to chronological age levels in OSK AD mice.

(E and F) Principal-component analysis (E) of spatial learning performance and clustering for all trained mice ($N = 105$, single dots), highlighting the group centroids (colored stars). Different ages, genotypes, and treatments are color coded as indicated. Note the displacement of the centroid of OSK-injected mice in each group toward that of young GFP-injected mice (quantified in F). Data are represented as correlation (A) and bar graphs (D, mean ± SD), as well as principal-component plots, with individual dots indicating mice (E) or groups of mice (F). $^{**}p < 0.01$; $^{*}p < 0.05$; ns, non-significant, by tests as indicated in Table S7.

See also Figure S10.

Next, we interrogated whether the cognitive clock would also reflect cognitive impairments in AD and, by extension, improvements upon AD engram reprogramming. For this, we used the water maze learning data from APP/PS1 (Figure 2) and, additionally, 5xFAD mice, another mouse model of AD expressing five AD-linked human mutations.[65] Similar to APP/PS1 mice, 5xFAD mice showed impairments in navigational learning, especially at the level of spatial precision (Figures S10E and S10F), which were rescued upon DG engram reprogramming (Figure S10G and S10H). We found that GFP-injected APP/PS1 and 5xFAD animals ($N = 11$ each) showed a significant increase in predicted vs. chronological age (Figures 5C, left, and 5D), reflecting an accelerated ticking of the cognitive clock in AD mice. In contrast, predicted age returned to chronological age levels in OSK-injected APP/PS1 and 5xFAD mice ($N = 13$ and 12, respectively, Figures 5C, right, and 5D), recapitulating the rejuvenating effect upon engram reprogramming in the context of AD (Figure S10I). Importantly, non-spatial parameters contained within the clock to predict age, such as swimming speed, were not changed in OSK-injected mice (Figure S10J), suggesting that OSK-derived cognitive improvements are the result of rejuvenated learning patterns rather than improved physical fitness. Thus, the cognitive clock developed here can accurately predict cognitive decline associated with both age and AD, as well as cognitive rejuvenation upon partial engram reprogramming.

Lastly, in order to confirm this cognitive rejuvenation with a different method, we performed an unbiased dimensionality reduction analysis pooling all spatial metrics across groups of experiments ($N = 105$ mice). We found that spatial-learning-based clustering separated groups of individual mice, with principal component (PC)1 and PC2 mostly reflecting age and genotype, respectively (Figures 5E and S10K). Furthermore, we observed that middle-aged AD mouse lines clustered further

Please cite this article in press as: Berdugo-Vega et al., Cognitive rejuvenation through partial reprogramming of engram cells, Neuron (2025), https://doi.org/10.1016/j.neuron.2025.11.028

from the oldest WT mice in the PC1 space, supporting an accelerated aging in mice with AD pathology, whereas the two transgenic AD lines clustered away from each other in the PC2 space, supporting the presence of navigational impairments distinctive to each model. Remarkably, irrespective of age and disease stage, centroids of the clusters of all OSK-injected mice significantly moved away from their respective GFP-injected counterparts and toward that of young GFP-injected mice (Figure 5F). Altogether, these results reinforce the notion that partial engram reprogramming leads to cognitive rejuvenation across ages and in AD.

DISCUSSION

Here, we report that partial reprogramming of engram cells by OSK-mediated gene therapy results in cognitive rejuvenation through changes at the cellular, molecular, electrophysiological, and behavioral level. These beneficial effects occurred in two conditions characterized by cognitive decline, i.e., in aged mice and mouse models of AD; were observed irrespective of the targeted brain area, i.e., the DG and mPFC; and did not lead to a loss in cellular identity but rather to a strengthening thereof. Together with a recent report of recovered vision in a mouse model of blindness upon expression of OSK in retinal ganglion cells,[7] this study suggests that higher-order brain functions, i.e., memory, can be successfully restored when OSK is targeted to the underlying impaired cell type, i.e., engram cells.

Directing molecular rejuvenation to the impaired neuronal subpopulation represents a significant advantage over less specific and longer-lasting approaches, for which cognitive improvements can be confounded by motor or systemic factors and which present an increased risk of de-differentiation by manipulating more cells for extended periods of time, respectively. As such, the engram-specific rescue strategy presented here expands previous reprogramming approaches at the whole-body or tissue level, which were shown to delay the onset of age-related memory impairments[9–13] but were started before the onset of cognitive decline and lasted for several months. Importantly, the present findings show that the controlled expression of OSK achieved by a one-time induction wave at the time of learning is sufficient for cellular rejuvenation while at the same time preventing de-differentiation.

For engrams in the context of aging and AD, this implies that cognitive capacities are not lost but merely constrained and can thus be recovered. Although similar results have been obtained when engram activity was temporarily and extrinsically reinstated by optogenetic activation for recent memories,[20,21] here engram function was more permanently reprogrammed, as evidenced by remote memory rescue. How long the beneficial effects of engram reprogramming can last beyond 2-week remote memories, and whether reprogrammed engrams cross-talk with neighboring cells or influence downstream circuits outside the targeted areas, remains, however, to be determined.

Upon OSK-mediated reprogramming, the transcriptional aberration of AD engram cells—comprising mainly synapse- and immune-response-related categories—was partly restored, although this restoration was most often not paralleled by alterations in chromatin accessibility. This could indicate that epigenetic changes induced by OSK occur at an earlier time and precede the transcriptional alterations, as has been reported for enhancer occupancy during full reprogramming.[48,50] Alternatively, OSK might affect other epigenetic modalities, such as H3K9me3, the overall levels of which were increased in reprogrammed engrams (Figures 1E and 1L), or DNA methylation, which is reportedly altered in both age and AD.[66,67]

Irrespective of its precise epigenetic mechanisms, our findings indicate that partial engram reprogramming likely rectifies signs of epigenetic erosion in age[68] and AD.[41] This is exemplified by the epigenetic and transcriptional profile of *Kcnj3* upon OSK treatment (Figure 3P), which directly translated into rescued engram hyperexcitability in AD (Figure 4). Because neuronal excitability is a prerequisite for proper engram functioning and memory recall,[58,69] but notoriously increased in AD,[60–63] it is likely that AD-related memory impairments were restored because of epigenetically altered electrophysiological properties of reprogrammed engrams. In turn, this implies that epigenetic engram plasticity is a prerequisite for proper mnemonic functions not only in the healthy[59,70] but also in the AD brain.

Lastly, in trying to better understand the nature of OSK-derived memory improvements, we developed a cognitive clock that was sensitive to memory decline and rescue. This clock allowed us to recognize OSK-mediated behavioral changes not just as mere improvements in discrete parameters but rather as a re-adoption of learning patterns typical of young mice, suggesting cognitive rejuvenation even upon reprogramming of a sparse engram population. By extension, this clock also provides a non-invasive biomarker to detect the presence of age-related deficits in mice, which could be used to quantify the effect of different therapeutic approaches or be applied in other disease models.

Taken together, our findings provide a proof of concept that targeting OSK to engram cells in the aged and diseased brain can help to recover cognitive functions. Although far from being readily translatable, such cell-type-specific approaches could in future studies also be applied to engrams with different functions, such as those in the insular cortex that coordinate immune responses,[71] to different cell types constrained in memory deterioration, or to different neurological disorders characterized by cognitive impairments.

Limitations of the study

In this study, we have exclusively used amyloid AD mouse models, as opposed to tau models, for which disease progression and underlying pathophysiological changes differ. In addition, our multi-omic and electrophysiological investigation of engram reprogramming has been restricted to a single time point (2 weeks after OSK-induction) and focused exclusively on AD-dependent changes and rescues thereof. Thus, the extent to which some of the beneficial phenotypes are secondary to other transcriptional and accessibility changes triggered by OSK was not investigated. Given our engram-targeting approach, we cannot exclude the possibility that a small fraction of non-reprogrammed cells were identified as engrams in our sequencing experiment, thus diluting our effects. Future work should additionally explore molecular changes occurring early after OSK induction and include young animals to unravel OSK's mode of

Please cite this article in press as: Berdugo-Vega et al., Cognitive rejuvenation through partial reprogramming of engram cells, Neuron (2025), https://doi.org/10.1016/j.neuron.2025.11.028

CellPress
OPEN ACCESS

action at even higher resolution. Further, including different cell types such as DG engrams in these analyses would hint at whether OSK induces cell-type-specific or cell-type-agnostic rejuvenation trajectories. Finally, while fear conditioning and spatial learning are commonly used to assess cognitive decline, the effect of engram reprogramming in behavioral tests less commonly used in the engram field, such as novel object recognition tasks, was not addressed.

RESOURCE AVAILABILITY

Lead contact

Requests for further information and resources should be directed to and will be fulfilled by the lead contact, Johannes Gräff (johannes.graeff@epfl.ch).

Materials availability

All unique/stable reagents generated in this study are available from the lead contact upon request, with a completed materials transfer agreement.

Data and code availability

- Single-nucleus multiome data have been deposited to GEO: GSE276656 and are publicly available as of the date of publication.
- All original code has been deposited to https://github.com/cesarsierran/multiome_OSK.
- Any additional information required to reanalyze the data reported in this paper is available from the lead contact upon request.

ACKNOWLEDGMENTS

This work was supported by the following funding bodies and grants to J.G.: Synapsis/Dementia Research Switzerland Foundation (2022-PI01), Secrétariat d'Etat à la formation à la recherche et à l'innovation (SEFRI, M822.00049), and Swiss National Science Foundation (310030_219342) and an EMBO Postdoctoral Fellowship (ALTF 64-2021) awarded to G.B.-V. The authors would like to thank Allison M. Burns, Rebecca Toscano-Rivalta, Austeja Dapkute, Irene Ferreres, and Myriam Schioppa for technical assistance; Bernard Schneider for insightful discussions and the Bertarelli Foundation Gene Therapy Platform for virus production; the EPFL's Center of Phenogenomics for ensuring animal welfare; the Histology Core Facility for support with brain sectioning and staining; the Bioimaging and Optic Core Facility for their expertise during image analysis; and the Gene Expression Core Facility for performing the sequencing experiment. The authors would also like to thank all present and past members of the Gräff lab for scientific feedback, insightful discussions, and their friendship. Last, G.B.-V. would like to dedicate this work to the memory of his father, Professor Javier Berdugo, who is deeply missed every day.

AUTHOR CONTRIBUTIONS

This work was conceptualized by J.G. and planned together with G.B.-V. G.B.-V. performed and analyzed all experiments, supported by V.C., J.O., and M.J.S. C. Sierra analyzed the multiome experiment and led its interpretation. S.A. planned and performed electrophysiology experiments, supervised by C. Sandi. The paper was written by G.B.-V. and J.G. and commented on by all authors. Correspondence should be addressed to G.B.-V. and J.G.

DECLARATION OF INTERESTS

The authors declare no competing interests.

STAR★METHODS

Detailed methods are provided in the online version of this paper and include the following:

- KEY RESOURCES TABLE
- EXPERIMENTAL MODEL AND STUDY PARTICIPANTS DETAILS
  - Mice
- METHOD DETAILS
  - Cloning, viral constructs and stereotaxic injections
  - Fear conditioning
  - Water maze
  - *Ex vivo* electrophysiology
  - Principal-component analysis and cognitive clock
  - Histology
  - Nuclei preparation for 10x multi-omics
- QUANTIFICATION AND STATISTICAL ANALYSIS
  - Imaging and quantifications
  - Statistics and reproducibility
  - 10X data processing and quality control
  - Dimensionality reduction and cell type identification
  - Cellular proportion analysis
  - Differential expression analysis
  - Generation of identity, engram and AD engram scores
  - Gene Ontology and gene set enrichment analysis
  - Differential accessibility analysis
  - Transcription factor motif enrichment, activity and footprint analysis
  - Gene expression - chromatin accessibility correlation

SUPPLEMENTAL INFORMATION

Supplemental information can be found online at https://doi.org/10.1016/j.neuron.2025.11.028.

Received: September 4, 2025
Revised: November 12, 2025
Accepted: November 26, 2025

REFERENCES

1. de Lima Camillo, L.P., and Quinlan, R.B.A. (2021). A ride through the epigenetic landscape: aging reversal by reprogramming. GeroScience *43*, 463–485. https://doi.org/10.1007/s11357-021-00358-6.
2. Yücel, A.D., and Gladyshev, V.N. (2024). The long and winding road of reprogramming-induced rejuvenation. Nat. Commun. *15*, 1941. https://doi.org/10.1038/s41467-024-46020-5.
3. Ocampo, A., Reddy, P., Martinez-Redondo, P., Platero-Luengo, A., Hatanaka, F., Hishida, T., Li, M., Lam, D., Kurita, M., Beyret, E., et al. (2016). In Vivo Amelioration of Age-Associated Hallmarks by Partial Reprogramming. Cell *167*, 1719–1733.e12. https://doi.org/10.1016/j.cell.2016.11.052.
4. Macip, C.C., Hasan, R., Hoznek, V., Kim, J., Lu, Y.R., Metzger, L.E., Sethna, S., and Davidsohn, N. (2024). Gene Therapy-Mediated Partial Reprogramming Extends Lifespan and Reverses Age-Related Changes in Aged Mice. Cell. Reprogramming *26*, 24–32. https://doi.org/10.1089/cell.2023.0072.
5. Hishida, T., Yamamoto, M., Hishida-Nozaki, Y., Shao, C., Huang, L., Wang, C., Shojima, K., Xue, Y., Hang, Y., Shokhirev, M., et al. (2022). In vivo partial cellular reprogramming enhances liver plasticity and regeneration. Cell Rep. *39*, 110730. https://doi.org/10.1016/j.celrep.2022.110730.
6. Chen, Y., Lüttmann, F.F., Schoger, E., Schöler, H.R., Zelarayán, L.C., Kim, K.-P., Haigh, J.J., Kim, J., and Braun, T. (2021). Reversible reprogramming of cardiomyocytes to a fetal state drives heart regeneration in mice. Science *373*, 1537–1540. https://doi.org/10.1126/science.abg5159.
7. Lu, Y., Brommer, B., Tian, X., Krishnan, A., Meer, M., Wang, C., Vera, D.L., Zeng, Q., Yu, D., Bonkowski, M.S., et al. (2020). Reprogramming to recover youthful epigenetic information and restore vision. Nature *588*, 124–129. https://doi.org/10.1038/s41586-020-2975-4.

Please cite this article in press as: Berdugo-Vega et al., Cognitive rejuvenation through partial reprogramming of engram cells, Neuron (2025), https://doi.org/10.1016/j.neuron.2025.11.028

8. Karg, M.M., Lu, Y.R., Refaian, N., Cameron, J., Hoffmann, E., Hoppe, C., Shirahama, S., Shah, M., Krasniqi, D., Krishnan, A., et al. (2023). Sustained Vision Recovery by OSK Gene Therapy in a Mouse Model of Glaucoma. Cell. Reprogramming *25*, 288–299. https://doi.org/10.1089/cell.2023.0074.

9. Rodríguez-Matellán, A., Alcazar, N., Hernández, F., Serrano, M., and Ávila, J. (2020). In Vivo Reprogramming Ameliorates Aging Features in Dentate Gyrus Cells and Improves Memory in Mice. Stem Cell Rep. *15*, 1056–1066. https://doi.org/10.1016/j.stemcr.2020.09.010.

10. Antón-Fernández, A., Roldán-Lázaro, M., Vallés-Saiz, L., Ávila, J., and Hernández, F. (2024). In vivo cyclic overexpression of Yamanaka factors restricted to neurons reverses age-associated phenotypes and enhances memory performance. Commun. Biol. *7*, 631. https://doi.org/10.1038/s42003-024-06328-w.

11. Shen, Y.-R., Zaballa, S., Bech, X., Sancho-Balsells, A., Rodríguez-Navarro, I., Cifuentes-Díaz, C., Seyit-Bremer, G., Chun, S.H., Straub, T., Abante, J., et al. (2024). Expansion of the neocortex and protection from neurodegeneration by in vivo transient reprogramming. Cell Stem Cell *31*, 1741–1759.e8. https://doi.org/10.1016/j.stem.2024.09.013.

12. Horvath, S., Lacunza, E., Mallat, M.C., Portiansky, E.L., Gallardo, M.D., Brooke, R.T., Chiavellini, P., Pasquini, D.C., Girard, M., Lehmann, M., et al. (2025). Cognitive rejuvenation in old rats by hippocampal OSKM gene therapy. GeroScience *47*, 809–823. https://doi.org/10.1007/s11357-024-01269-y.

13. Antón-Fernández, A., Ruiz de Alegría, Á., Mariscal-Casero, A., Roldán-Lázaro, M., Peinado-Cauchola, R., Ávila, J., and Hernández, F. (2025). Partial reprogramming by cyclical overexpression of Yamanaka factors improves pathological phenotypes of tauopathy mouse model of human Alzheimer's disease. Prog. Neurobiol. *247*, 102743. https://doi.org/10.1016/j.pneurobio.2025.102743.

14. Josselyn, S.A., Köhler, S., and Frankland, P.W. (2015). Finding the engram. Nat. Rev. Neurosci. *16*, 521–534. https://doi.org/10.1038/nrn4000.

15. Josselyn, S.A., and Tonegawa, S. (2020). Memory engrams: Recalling the past and imagining the future. Science *367*, eaaw4325. https://doi.org/10.1126/science.aaw4325.

16. Denny, C.A., Kheirbek, M.A., Alba, E.L., Tanaka, K.F., Brachman, R.A., Laughman, K.B., Tomm, N.K., Turi, G.F., Losonczy, A., and Hen, R. (2014). Hippocampal Memory Traces Are Differentially Modulated by Experience, Time, and Adult Neurogenesis. Neuron *83*, 189–201. https://doi.org/10.1016/j.neuron.2014.05.018.

17. Liu, X., Ramirez, S., Pang, P.T., Puryear, C.B., Govindarajan, A., Deisseroth, K., and Tonegawa, S. (2012). Optogenetic stimulation of a hippocampal engram activates fear memory recall. Nature *484*, 381–385. https://doi.org/10.1038/nature11028.

18. Kitamura, T., Ogawa, S.K., Roy, D.S., Okuyama, T., Morrissey, M.D., Smith, L.M., Redondo, R.L., and Tonegawa, S. (2017). Engrams and circuits crucial for systems consolidation of a memory. Science *356*, 73–78. https://doi.org/10.1126/science.aam6808.

19. DeNardo, L.A., Liu, C.D., Allen, W.E., Adams, E.L., Friedmann, D., Fu, L., Guenthner, C.J., Tessier-Lavigne, M., and Luo, L. (2019). Temporal evolution of cortical ensembles promoting remote memory retrieval. Nat. Neurosci. *22*, 460–469. https://doi.org/10.1038/s41593-018-0318-7.

20. Roy, D.S., Arons, A., Mitchell, T.I., Pignatelli, M., Ryan, T.J., and Tonegawa, S. (2016). Memory retrieval by activating engram cells in mouse models of early Alzheimer's disease. Nature *531*, 508–512. https://doi.org/10.1038/nature17172.

21. Perusini, J.N., Cajigas, S.A., Cohensedgh, O., Lim, S.C., Pavlova, I.P., Donaldson, Z.R., and Denny, C.A. (2017). Optogenetic stimulation of dentate gyrus engrams restores memory in Alzheimer's disease mice. Hippocampus *27*, 1110–1122. https://doi.org/10.1002/hipo.22756.

22. Poll, S., Mittag, M., Musacchio, F., Justus, L.C., Giovannetti, E.A., Steffen, J., Wagner, J., Zohren, L., Schoch, S., Schmidt, B., et al. (2020). Memory trace interference impairs recall in a mouse model of Alzheimer's disease. Nat. Neurosci. *23*, 952–958. https://doi.org/10.1038/s41593-020-0652-4.

23. Gulmez Karaca, K., Brito, D.V.C., Kupke, J., Zeuch, B., and Oliveira, A.M.M. (2021). Engram reactivation during memory retrieval predicts long-term memory performance in aged mice. Neurobiol. Aging *101*, 256–261. https://doi.org/10.1016/j.neurobiolaging.2021.01.019.

24. Iwano, T., Masuda, A., Kiyonari, H., Enomoto, H., and Matsuzaki, F. (2012). Prox1 postmitotically defines dentate gyrus cells by specifying granule cell identity over CA3 pyramidal cell fate in the hippocampus. Development *139*, 3051–3062. https://doi.org/10.1242/dev.080002.

25. Pal, S., and Tyler, J.K. (2016). Epigenetics and aging. Sci. Adv. *2*, e1600584. https://doi.org/10.1126/sciadv.1600584.

26. Zhang, Y., Amaral, M.L., Zhu, C., Grieco, S.F., Hou, X., Lin, L., Buchanan, J., Tong, L., Preissl, S., Xu, X., et al. (2022). Single-cell epigenome analysis reveals age-associated decay of heterochromatin domains in excitatory neurons in the mouse brain. Cell Res. *32*, 1008–1021. https://doi.org/10.1038/s41422-022-00719-6.

27. Matias, I., Diniz, L.P., Damico, I.V., Araujo, A.P.B., Neves, L.D.S., Vargas, G., Leite, R.E.P., Suemoto, C.K., Nitrini, R., Jacob-Filho, W., et al. (2022). Loss of lamin-B1 and defective nuclear morphology are hallmarks of astrocyte senescence in vitro and in the aging human hippocampus. Aging Cell *21*, e13521. https://doi.org/10.1111/acel.13521.

28. Frey, T., Murakami, T., Maki, K., Kawaue, T., Tani, N., Sugai, A., Nakazawa, N., Ishiguro, K.I., Adachi, T., Kengaku, M., et al. (2023). Age-associated reduction of nuclear shape dynamics in excitatory neurons of the visual cortex. Aging Cell *22*, e13925. https://doi.org/10.1111/acel.13925.

29. Das, S., and Ramanan, N. (2023). Region-specific heterogeneity in neuronal nuclear morphology in young, aged and in Alzheimer's disease mouse brains. Front. Cell Dev. Biol. *11*, 1032504. https://doi.org/10.3389/fcell.2023.1032504.

30. Borchelt, D.R., Ratovitski, T., van Lare, J., Lee, M.K., Gonzales, V., Jenkins, N.A., Copeland, N.G., Price, D.L., and Sisodia, S.S. (1997). Accelerated Amyloid Deposition in the Brains of Transgenic Mice Coexpressing Mutant Presenilin 1 and Amyloid Precursor Proteins. Neuron *19*, 939–945. https://doi.org/10.1016/S0896-6273(00)80974-5.

31. Islam, M.I., Nagakannan, P., Shcholok, T., Contu, F., Mai, S., Albensi, B.C., Del Bigio, M.R., Wang, J.-F., Sharoar, M.G., Yan, R., et al. (2022). Regulatory role of cathepsin L in induction of nuclear laminopathy in Alzheimer's disease. Aging Cell *21*, e13531. https://doi.org/10.1111/acel.13531.

32. Hulshof, L.A., Frajmund, L.A., van Nuijs, D., van der Heijden, D.C.N., Middeldorp, J., and Hol, E.M. (2022). Both male and female APPswe/PSEN1dE9 mice are impaired in spatial memory and cognitive flexibility at 9 months of age. Neurobiol. Aging *113*, 28–38. https://doi.org/10.1016/j.neurobiolaging.2021.12.009.

33. Lalonde, R., Kim, H.D., Maxwell, J.A., and Fukuchi, K. (2005). Exploratory activity and spatial learning in 12-month-old *APP*695SWE/co + *PS1*/ΔE9 mice with amyloid plaques. Neurosci. Lett. *390*, 87–92. https://doi.org/10.1016/j.neulet.2005.08.028.

34. O'Leary, T.P., and Brown, R.E. (2009). Visuo-spatial learning and memory deficits on the Barnes maze in the 16-month-old APPswe/PS1dE9 mouse model of Alzheimer's disease. Behav. Brain Res. *201*, 120–127. https://doi.org/10.1016/j.bbr.2009.01.039.

35. Berdugo-Vega, G., Arias-Gil, G., López-Fernández, A., Artegiani, B., Wasielewska, J.M., Lee, C.-C., Lippert, M.T., Kempermann, G., Takagaki, K., and Calegari, F. (2020). Increasing neurogenesis refines hippocampal activity rejuvenating navigational learning strategies and contextual memory throughout life. Nat. Commun. *11*, 135. https://doi.org/10.1038/s41467-019-14026-z.

36. Garthe, A., and Kempermann, G. (2013). An old test for new neurons: refining the Morris water maze to study the functional relevance of adult hippocampal neurogenesis. Front. Neurosci. *7*, 63. https://doi.org/10.3389/fnins.2013.00063.

37. Yao, Z., van Velthoven, C.T.J., Nguyen, T.N., Goldy, J., Sedeno-Cortes, A.E., Baftizadeh, F., Bertagnolli, D., Casper, T., Chiang, M., Crichton, K.,

Please cite this article in press as: Berdugo-Vega et al., Cognitive rejuvenation through partial reprogramming of engram cells, Neuron (2025), https://doi.org/10.1016/j.neuron.2025.11.028

et al. (2021). A taxonomy of transcriptomic cell types across the isocortex and hippocampal formation. Cell *184*, 3222–3241.e26. https://doi.org/10.1016/j.cell.2021.04.021.

38. Bhattacherjee, A., Zhang, C., Watson, B.R., Djekidel, M.N., Moffitt, J.R., and Zhang, Y. (2023). Spatial transcriptomics reveals the distinct organization of mouse prefrontal cortex and neuronal subtypes regulating chronic pain. Nat. Neurosci. *26*, 1880–1893. https://doi.org/10.1038/s41593-023-01455-9.

39. Mertens, J., Herdy, J.R., Traxler, L., Schafer, S.T., Schlachetzki, J.C.M., Böhnke, L., Reid, D.A., Lee, H., Zangwill, D., Fernandes, D.P., et al. (2021). Age-dependent instability of mature neuronal fate in induced neurons from Alzheimer's patients. Cell Stem Cell *28*, 1533–1548.e6. https://doi.org/10.1016/j.stem.2021.04.004.

40. Caldwell, A.B., Liu, Q., Schroth, G.P., Galasko, D.R., Yuan, S.H., Wagner, S.L., and Subramaniam, S. (2020). Dedifferentiation and neuronal repression define familial Alzheimer's disease. Sci. Adv. *6*, eaba5933. https://doi.org/10.1126/sciadv.aba5933.

41. Xiong, X., James, B.T., Boix, C.A., Park, Y.P., Galani, K., Victor, M.B., Sun, N., Hou, L., Ho, L.-L., Mantero, J., et al. (2023). Epigenomic dissection of Alzheimer's disease pinpoints causal variants and reveals epigenome erosion. Cell *186*, 4422–4437.e21. https://doi.org/10.1016/j.cell.2023.08.040.

42. Mouton-Liger, F., Dumurgier, J., Cognat, E., Hourregue, C., Zetterberg, H., Vanderstichele, H., Vanmechelen, E., Bouaziz-Amar, E., Blennow, K., Hugon, J., et al. (2020). CSF levels of the BACE1 substrate NRG1 correlate with cognition in Alzheimer's disease. Alzheimers Res. Ther. *12*, 88. https://doi.org/10.1186/s13195-020-00655-w.

43. Ryu, J., Hong, B.H., Kim, Y.J., Yang, E.J., Choi, M., Kim, H., Ahn, S., Baik, T.K., Woo, R.S., and Kim, H.S. (2016). Neuregulin-1 attenuates cognitive function impairments in a transgenic mouse model of Alzheimer's disease. Cell Death Dis. *7*, e2117. https://doi.org/10.1038/cddis.2016.30.

44. Cui, W., Tao, J., Wang, Z., Ren, M., Zhang, Y., Sun, Y., Peng, Y., and Li, R. (2013). Neuregulin1beta1 Antagonizes Apoptosis Via ErbB4-Dependent Activation of PI3-Kinase/Akt in APP/PS1 Transgenic Mice. Neurochem. Res. *38*, 2237–2246. https://doi.org/10.1007/s11064-013-1131-z.

45. Salazar, S.V., Gallardo, C., Kaufman, A.C., Herber, C.S., Haas, L.T., Robinson, S., Manson, J.C., Lee, M.K., and Strittmatter, S.M. (2017). Conditional Deletion of Prnp Rescues Behavioral and Synaptic Deficits after Disease Onset in Transgenic Alzheimer's Disease. J. Neurosci. *37*, 9207–9221. https://doi.org/10.1523/JNEUROSCI.0722-17.2017.

46. Keenan, A.B., Torre, D., Lachmann, A., Leong, A.K., Wojciechowicz, M.L., Utti, V., Jagodnik, K.M., Kropiwnicki, E., Wang, Z., and Ma'ayan, A. (2019). ChEA3: transcription factor enrichment analysis by orthogonal omics integration. Nucleic Acids Res. *47*, W212–W224. https://doi.org/10.1093/nar/gkz446.

47. Donaghey, J., Thakurela, S., Charlton, J., Chen, J.S., Smith, Z.D., Gu, H., Pop, R., Clement, K., Stamenova, E.K., Karnik, R., et al. (2018). Genetic determinants and epigenetic effects of pioneer-factor occupancy. Nat. Genet. *50*, 250–258. https://doi.org/10.1038/s41588-017-0034-3.

48. Chronis, C., Fiziev, P., Papp, B., Butz, S., Bonora, G., Sabri, S., Ernst, J., and Plath, K. (2017). Cooperative Binding of Transcription Factors Orchestrates Reprogramming. Cell *168*, 442–459.e20. https://doi.org/10.1016/j.cell.2016.12.016.

49. Pardo, M., Lang, B., Yu, L., Prosser, H., Bradley, A., Babu, M.M., and Choudhary, J. (2010). An Expanded Oct4 Interaction Network: Implications for Stem Cell Biology, Development, and Disease. Cell Stem Cell *6*, 382–395. https://doi.org/10.1016/j.stem.2010.03.004.

50. Soufi, A., Donahue, G., and Zaret, K.S. (2012). Facilitators and Impediments of the Pluripotency Reprogramming Factors' Initial Engagement with the Genome. Cell *151*, 994–1004. https://doi.org/10.1016/j.cell.2012.09.045.

51. Jeremic, D., Sanchez-Rodriguez, I., Jimenez-Diaz, L., and Navarro-Lopez, J.D. (2021). Therapeutic potential of targeting G protein-gated inwardly rectifying potassium (GIRK) channels in the central nervous system. Pharmacol. Ther. *223*, 107808. https://doi.org/10.1016/j.pharmthera.2021.107808.

52. Mett, A., Karbat, I., Tsoory, M., Fine, S., Iwanir, S., and Reuveny, E. (2021). Reduced activity of GIRK1-containing heterotetramers is sufficient to affect neuronal functions, including synaptic plasticity and spatial learning and memory. J. Physiol. *599*, 521–545. https://doi.org/10.1113/JP280434.

53. Djebari, S., Iborra-Lázaro, G., Temprano-Carazo, S., Sánchez-Rodríguez, I., Nava-Mesa, M.O., Múnera, A., Gruart, A., Delgado-García, J.M., Jiménez-Díaz, L., and Navarro-López, J.D. (2021). G-Protein-Gated Inwardly Rectifying Potassium (Kir3/GIRK) Channels Govern Synaptic Plasticity That Supports Hippocampal-Dependent Cognitive Functions in Male Mice. J. Neurosci. *41*, 7086–7102. https://doi.org/10.1523/JNEUROSCI.2849-20.2021.

54. Sánchez-Rodríguez, I., Djebari, S., Temprano-Carazo, S., Vega-Avelaira, D., Jiménez-Herrera, R., Iborra-Lázaro, G., Yajeya, J., Jiménez-Díaz, L., and Navarro-López, J.D. (2020). Hippocampal long-term synaptic depression and memory deficits induced in early amyloidopathy are prevented by enhancing G-protein-gated inwardly rectifying potassium channel activity. J. Neurochem. *153*, 362–376. https://doi.org/10.1111/jnc.14946.

55. Sánchez-Rodríguez, I., Temprano-Carazo, S., Nájera, A., Djebari, S., Yajeya, J., Gruart, A., Delgado-García, J.M., Jiménez-Díaz, L., and Navarro-López, J.D. (2017). Activation of G-protein-gated inwardly rectifying potassium (Kir3/GirK) channels rescues hippocampal functions in a mouse model of early amyloid-β pathology. Sci. Rep. *7*, 14658. https://doi.org/10.1038/s41598-017-15306-8.

56. Yiu, A.P., Mercaldo, V., Yan, C., Richards, B., Rashid, A.J., Hsiang, H.-L.L., Pressey, J., Mahadevan, V., Tran, M.M., Kushner, S.A., et al. (2014). Neurons Are Recruited to a Memory Trace Based on Relative Neuronal Excitability Immediately before Training. Neuron *83*, 722–735. https://doi.org/10.1016/j.neuron.2014.07.017.

57. Lau, J.M.H., Rashid, A.J., Jacob, A.D., Frankland, P.W., Schacter, D.L., and Josselyn, S.A. (2020). The role of neuronal excitability, allocation to an engram and memory linking in the behavioral generation of a false memory in mice. Neurobiol. Learn. Mem. *174*, 107284. https://doi.org/10.1016/j.nlm.2020.107284.

58. Pignatelli, M., Ryan, T.J., Roy, D.S., Lovett, C., Smith, L.M., Muralidhar, S., and Tonegawa, S. (2019). Engram Cell Excitability State Determines the Efficacy of Memory Retrieval. Neuron *101*, 274–284.e5. https://doi.org/10.1016/j.neuron.2018.11.029.

59. Santoni, G., Astori, S., Leleu, M., Glauser, L., Zamora, S.A., Schioppa, M., Tarulli, I., Sandi, C., and Gräff, J. (2024). Chromatin plasticity predetermines neuronal eligibility for memory trace formation. Science *385*, eadg9982. https://doi.org/10.1126/science.adg9982.

60. Kellner, V., Menkes-Caspi, N., Beker, S., and Stern, E.A. (2014). Amyloid-β alters ongoing neuronal activity and excitability in the frontal cortex. Neurobiol. Aging *35*, 1982–1991. https://doi.org/10.1016/j.neurobiolaging.2014.04.001.

61. Šišková, Z., Justus, D., Kaneko, H., Friedrichs, D., Henneberg, N., Beutel, T., Pitsch, J., Schoch, S., Becker, A., von der Kammer, H., et al. (2014). Dendritic Structural Degeneration Is Functionally Linked to Cellular Hyperexcitability in a Mouse Model of Alzheimer's Disease. Neuron *84*, 1023–1033. https://doi.org/10.1016/j.neuron.2014.10.024.

62. Torres-Flores, M., and Peña-Ortega, F. (2022). Amyloid Beta Alters Prefrontal-dependent Functions Along with its Excitability and Synaptic Plasticity in Male Rats. Neuroscience *498*, 260–279. https://doi.org/10.1016/j.neuroscience.2022.07.006.

63. Choudhury, N., Chen, L., Al-Harthi, L., and Hu, X.-T. (2023). Hyperactivity of medial prefrontal cortex pyramidal neurons occurs in a mouse model

Please cite this article in press as: Berdugo-Vega et al., Cognitive rejuvenation through partial reprogramming of engram cells, Neuron (2025), https://doi.org/10.1016/j.neuron.2025.11.028

of early-stage Alzheimer's disease without β-amyloid accumulation. Front. Pharmacol. *14*, 1194869. https://doi.org/10.3389/fphar.2023.1194869.

64. Anderson, E.M., Demis, S., Wrucke, B., Engelhardt, A., and Hearing, M.C. (2021). Infralimbic cortex pyramidal neuron GIRK signaling contributes to regulation of cognitive flexibility but not affect-related behavior in male mice. Physiol. Behav. *242*, 113597. https://doi.org/10.1016/j.physbeh.2021.113597.

65. Oakley, H., Cole, S.L., Logan, S., Maus, E., Shao, P., Craft, J., Guillozet-Bongaarts, A., Ohno, M., Disterhoft, J., Van Eldik, L.V., et al. (2006). Intraneuronal β-Amyloid Aggregates, Neurodegeneration, and Neuron Loss in Transgenic Mice with Five Familial Alzheimer's Disease Mutations: Potential Factors in Amyloid Plaque Formation. J. Neurosci. *26*, 10129–10140. https://doi.org/10.1523/JNEUROSCI.1202-06.2006.

66. Coninx, E., Chew, Y.C., Yang, X., Guo, W., Coolkens, A., Baatout, S., Moons, L., Verslegers, M., and Quintens, R. (2020). Hippocampal and cortical tissue-specific epigenetic clocks indicate an increased epigenetic age in a mouse model for Alzheimer's disease. Aging *12*, 20817–20834. https://doi.org/10.18632/aging.104056.

67. Horvath, S., and Raj, K. (2018). DNA methylation-based biomarkers and the epigenetic clock theory of ageing. Nat. Rev. Genet. *19*, 371–384. https://doi.org/10.1038/s41576-018-0004-3.

68. Yang, J.-H., Hayano, M., Griffin, P.T., Amorim, J.A., Bonkowski, M.S., Apostolides, J.K., Salfati, E.L., Blanchette, M., Munding, E.M., Bhakta, M., et al. (2023). Loss of epigenetic information as a cause of mammalian aging. Cell *186*, 305–326.e27. https://doi.org/10.1016/j.cell.2022.12.027.

69. Albo, Z., and Gräff, J. (2018). The mysteries of remote memory. Philos. Trans. R. Soc. Lond. B Biol. Sci. *373*, 20170029. https://doi.org/10.1098/rstb.2017.0029.

70. Coda, D.M., Watt, L., Glauser, L., Batiuk, M.Y., Burns, A.M., Stahl, C.L., Wong, L.Y., and Gräff, J. (2025). Cell-type- and locus-specific epigenetic editing of memory expression. Nat. Genet. *57*, 2661–2668. https://doi.org/10.1038/s41588-025-02368-y.

71. Koren, T., Yifa, R., Amer, M., Krot, M., Boshnak, N., Ben-Shaanan, T.L., Azulay-Debby, H., Zalayat, I., Avishai, E., Hajjo, H., et al. (2021). Insular cortex neurons encode and retrieve specific immune responses. Cell *184*, 5902–5915.e17. https://doi.org/10.1016/j.cell.2021.10.013.

72. Bankhead, P., Loughrey, M.B., Fernández, J.A., Dombrowski, Y., McArt, D.G., Dunne, P.D., McQuaid, S., Gray, R.T., Murray, L.J., Coleman, H.G., et al. (2017). QuPath: Open source software for digital pathology image analysis. Sci. Rep. *7*, 16878. https://doi.org/10.1038/s41598-017-17204-5.

73. Velychko, S., Adachi, K., Kim, K.-P., Hou, Y., MacCarthy, C.M., Wu, G., and Schöler, H.R. (2019). Excluding Oct4 from Yamanaka Cocktail Unleashes the Developmental Potential of iPSCs. Cell Stem Cell *25*, 737–753.e4. https://doi.org/10.1016/j.stem.2019.10.002.

74. Choi, J.-H., Yu, N.-K., Baek, G.-C., Bakes, J., Seo, D., Nam, H.J., Baek, S.H., Lim, C.-S., Lee, Y.-S., and Kaang, B.-K. (2014). Optimization of AAV expression cassettes to improve packaging capacity and transgene expression in neurons. Mol. Brain *7*, 17. https://doi.org/10.1186/1756-6606-7-17.

75. Zhang, Z., Ferretti, V., Güntan, İ., Moro, A., Steinberg, E.A., Ye, Z., Zecharia, A.Y., Yu, X., Vyssotski, A.L., Brickley, S.G., et al. (2015). Neuronal ensembles sufficient for recovery sleep and the sedative actions of α2 adrenergic agonists. Nat. Neurosci. *18*, 553–561. https://doi.org/10.1038/nn.3957.

76. Dixsaut, L., and Gräff, J. (2022). Brain-wide screen of prelimbic cortex inputs reveals a functional shift during early fear memory consolidation. eLife *11*, e78542. https://doi.org/10.7554/eLife.78542.

77. Berdugo-Vega, G., Lee, C.-C., Garthe, A., Kempermann, G., and Calegari, F. (2021). Adult-born neurons promote cognitive flexibility by improving memory precision and indexing. Hippocampus *31*, 1068–1079. https://doi.org/10.1002/hipo.23373.

78. Overall, R.W., Zocher, S., Garthe, A., and Kempermann, G. (2020). Rtrack: a software package for reproducible automated water maze analysis. Preprint at bioRxiv. https://doi.org/10.1101/2020.02.27.967372.

79. Ting, J.T., Daigle, T.L., Chen, Q., and Feng, G. (2014). Acute brain slice methods for adult and aging animals: application of targeted patch clamp analysis and optogenetics. Methods Mol. Biol. *1183*, 221–242. https://doi.org/10.1007/978-1-4939-1096-0_14.

80. Batiuk, M.Y., Tyler, T., Dragicevic, K., Mei, S., Rydbirk, R., Petukhov, V., Deviatiiarov, R., Sedmak, D., Frank, E., Feher, V., et al. (2022). Upper cortical layer–driven network impairment in schizophrenia. Sci. Adv. *8*, eabn8367. https://doi.org/10.1126/sciadv.abn8367.

81. Hao, Y., Stuart, T., Kowalski, M.H., Choudhary, S., Hoffman, P., Hartman, A., Srivastava, A., Molla, G., Madad, S., Fernandez-Granda, C., et al. (2024). Dictionary learning for integrative, multimodal and scalable single-cell analysis. Nat. Biotechnol. *42*, 293–304. https://doi.org/10.1038/s41587-023-01767-y.

82. Stuart, T., Srivastava, A., Madad, S., Lareau, C.A., and Satija, R. (2021). Single-cell chromatin state analysis with Signac. Nat. Methods *18*, 1333–1341. https://doi.org/10.1038/s41592-021-01282-5.

83. Zhang, Y., Liu, T., Meyer, C.A., Eeckhoute, J., Johnson, D.S., Bernstein, B.E., Nusbaum, C., Myers, R.M., Brown, M., Li, W., et al. (2008). Model-based Analysis of ChIP-Seq (MACS). Genome Biol. *9*, R137. https://doi.org/10.1186/gb-2008-9-9-r137.

84. Aran, D., Looney, A.P., Liu, L., Wu, E., Fong, V., Hsu, A., Chak, S., Naikawadi, R.P., Wolters, P.J., Abate, A.R., et al. (2019). Reference-based analysis of lung single-cell sequencing reveals a transitional profibrotic macrophage. Nat. Immunol. *20*, 163–172. https://doi.org/10.1038/s41590-018-0276-y.

85. Fernández-Blanco, Á., Sierra, C., Tejido, C., and Dierssen, M. (2024). Beyond Quiescent and Active: Intermediate Microglial Transcriptomic States in a Mouse Model of Down Syndrome. Int. J. Mol. Sci. *25*, 3289. https://doi.org/10.3390/ijms25063289.

86. Reifschneider, A., Robinson, S., van Lengerich, B., Gnörich, J., Logan, T., Heindl, S., Vogt, M.A., Weidinger, E., Riedl, L., Wind, K., et al. (2022). Loss of TREM2 rescues hyperactivation of microglia, but not lysosomal deficits and neurotoxicity in models of progranulin deficiency. EMBO J. *41*, e109108. https://doi.org/10.15252/embj.2021109108.

87. Keren-Shaul, H., Spinrad, A., Weiner, A., Matcovitch-Natan, O., Dvir-Szternfeld, R., Ulland, T.K., David, E., Baruch, K., Lara-Astaiso, D., Toth, B., et al. (2017). A Unique Microglia Type Associated with Restricting Development of Alzheimer's Disease. Cell *169*, 1276–1290.e17. https://doi.org/10.1016/j.cell.2017.05.018.

88. Barres, B.A., Hart, I.K., Coles, H.S.R., Burne, J.F., Voyvodic, J.T., Richardson, W.D., and Raff, M.C. (1992). Cell death and control of cell survival in the oligodendrocyte lineage. Cell *70*, 31–46. https://doi.org/10.1016/0092-8674(92)90531-G.

89. Korsunsky, I., Millard, N., Fan, J., Slowikowski, K., Zhang, F., Wei, K., Baglaenko, Y., Brenner, M., Loh, P.R., and Raychaudhuri, S. (2019). Fast, sensitive and accurate integration of single-cell data with Harmony. Nat. Methods *16*, 1289–1296. https://doi.org/10.1038/s41592-019-0619-0.

90. Cao, Y., Lin, Y., Ormerod, J.T., Yang, P., Yang, J.Y.H., and Lo, K.K. (2019). scDC: single cell differential composition analysis. BMC Bioinform. *20*, 721. https://doi.org/10.1186/s12859-019-3211-9.

91. Junttila, S., Smolander, J., and Elo, L.L. (2022). Benchmarking methods for detecting differential states between conditions from multi-subject single-cell RNA-seq data. Brief. Bioinform. *23*, bbac286. https://doi.org/10.1093/bib/bbac286.

Please cite this article in press as: Berdugo-Vega et al., Cognitive rejuvenation through partial reprogramming of engram cells, Neuron (2025), https://doi.org/10.1016/j.neuron.2025.11.028

92. Qiu, X., Hill, A., Packer, J., Lin, D., Ma, Y.-A., and Trapnell, C. (2017). Single-cell mRNA quantification and differential analysis with Census. Nat. Methods *14*, 309–315. https://doi.org/10.1038/nmeth.4150.

93. Ge, S.X., Jung, D., and Yao, R. (2020). ShinyGO: a graphical gene-set enrichment tool for animals and plants. Bioinformatics *36*, 2628–2629. https://doi.org/10.1093/bioinformatics/btz931.

94. Yu, G., Wang, L.-G., and He, Q.-Y. (2015). ChIPseeker: an R/Bioconductor package for ChIP peak annotation, comparison and visualization. Bioinformatics *31*, 2382–2383. https://doi.org/10.1093/bioinformatics/btv145.

95. Fornes, O., Castro-Mondragon, J.A., Khan, A., van der Lee, R., Zhang, X., Richmond, P.A., Modi, B.P., Correard, S., Gheorghe, M., Baranašić, D., et al. (2020). JASPAR 2020: update of the open-access database of transcription factor binding profiles. Nucleic Acids Res. *48*, D87–D92. https://doi.org/10.1093/nar/gkz1001.

96. Schep, A.N., Wu, B., Buenrostro, J.D., and Greenleaf, W.J. (2017). chromVAR: inferring transcription-factor-associated accessibility from single-cell epigenomic data. Nat. Methods *14*, 975–978. https://doi.org/10.1038/nmeth.4401.

Please cite this article in press as: Berdugo-Vega et al., Cognitive rejuvenation through partial reprogramming of engram cells, Neuron (2025), https://doi.org/10.1016/j.neuron.2025.11.028

STAR★METHODS

KEY RESOURCES TABLE

REAGENT or RESOURCE	SOURCE	IDENTIFIER
Antibodies		
Goat anti-GFP	Abcam	Cat#ab6673; RRID:AB_305643
Rabbit anti-GFP	Abcam	Cat#ab290; RRID:AB_303395
Mouse anti-GFP	Abcam	Cat# ab1218; RRID:AB_298911
Goat anti-Klf4	R&D Systems	Cat# AF3158; RRID:AB_2130245
Guinea pig anti-cFos	Synaptic Systems	Cat# 226 308; RRID:AB_2905595
Rabbit anti-Prox1	Abcam	Cat# ab101851; RRID:AB_10712211
Rabbit anti-H3K9me3	Abcam	Cat# ab176916; RRID:AB_2797591
Rabbit anti-LaminB1	Abcam	Cat# ab229025; RRID:AB_3083735
Rat anti-Ctip2	Abcam	Cat# ab18465; RRID:AB_2064130
Donkey anti-goat AlexaFluor 488	Thermo Fisher	Cat# A-11055; RRID:AB_2534102
Donkey anti-rabbit AlexaFluor 488	Thermo Fisher	Cat# A-21206; RRID:AB_2535792
Donkey anti-mouse AlexaFluor 488	Thermo Fisher	Cat# A-21202; RRID:AB_141607
Donkey anti-goat AlexaFluor 568	Thermo Fisher	Cat# A-11057; RRID:AB_2534104
Donkey anti-guinea pig AlexaFluor 647	Jackson ImmunoResearch	Cat# 706-605-148; RRID:AB_2340476
Donkey anti-rabbit AlexaFluor 647	Thermo Fisher	Cat# A-31573; RRID:AB_2536183
Donkey anti-rat AlexaFluor 647	Thermo Fisher	Cat# A48272TR; RRID:AB_2896338
Goat anti-guinea pig AlexaFluor750	Abcam	Cat# ab175758
Bacterial and virus strains		
AAV8 TRE::OSK	This paper; produced at EPFL's Bertarelli Foundation Gene Therapy Platform	N/A
AAV8 cFos::tTA	EPFL's Bertarelli Foundation Gene Therapy Platform	Addgene plasmid #66794, gift from William Wisden
AAV8 TRE::GFP	UNC Vector Core	N/A
Chemicals, peptides, and recombinant proteins		
ML-297	Abcam	Cat# ab143564
Doxycycline	Sigma-Aldrich	Cat# CAS 24390-14-5
Streptavidine AlexaFluor 647	Thermo Fisher	Cat# S32357
TSA Opal520	Akoya Biosciences	Cat# FP1487001KT
TSA Opal570	Akoya Biosciences	Cat# FP1488001KT
TSA Opal650	Akoya Biosciences	Cat# FP1496001KT
Critical commercial assays		
RNA Scope Multiplex Fluorescent V2 kit	ACD Bio	N/A
Chromium Next GEM Single Cell Multiome ATAC + Gene Expression	10x Genomics	N/A
Deposited data		
Gene expression + ATAC multiome profiling of mPFC engram cells after OSK partial reprogramming	This paper	GEO: GSE276656
Code used to analyze the single-nuclei multiome dataset	This paper	github.com/cesarsierran/multiome_OSK
Experimental models: Organisms/strains		
Mouse APP/PS1 (B6.Cg-Tg(APPswe,PSEN1dE9)85Dbo/Mmjax)	Jackson Laboratory	MMRRC_034832-JAX
Mouse 5xFAD (B6.Cg-Tg(APPSwFlLon,PSEN1*M146L*L286V)6799Vas/Mmjax)	Jackson Laboratory	MMRRC_034848-JAX

(*Continued on next page*)

Please cite this article in press as: Berdugo-Vega et al., Cognitive rejuvenation through partial reprogramming of engram cells, Neuron (2025), https://doi.org/10.1016/j.neuron.2025.11.028

Continued

REAGENT or RESOURCE	SOURCE	IDENTIFIER
Oligonucleotides		
RNAscope™ HiPlex Probe - Mm-Pou5f1-O2	Bio-Techne	Cat# 1247361-C1
RNAscope™ HiPlex Probe - Mm Klf4-O1	Bio-Techne	Cat# 813851-C2
RNAscope™ HiPlex Probe - Mm Sox2-O1	Bio-Techne	Cat# 1247371-C3
Software and algorithms		
Qupath 0.5.1	Bankhead et al.[72]	N/A
Fiji (v2.14.0)	ImageJ	N/A
Adobe Illustrator 2025	Adobe	N/A
Adobe Photoshop 2025	Adobe	N/A
Graphpad prism 10	Graphpad	N/A
RStudio 2023.06.1	R	N/A
CellRanger-arc software (v2.0.0)	10x Genomics	N/A

EXPERIMENTAL MODEL AND STUDY PARTICIPANTS DETAILS

Mice

All animals and procedures were approved by the Veterinary Office of the Federal Council of Switzerland under the animal experimentation licenses VD3662. APP/PS1 and 5xFAD mouse lines were bred in house in the C57Bl/6JR background, and transgenic and non-transgenic (wild-type littermates) offspring of either sex was used as experimental mice at young (2–4 months), aged (9–10) or old age (18–20 months old). For behavior, fear conditioning experiments were performed in male WT mice (Figure 1), whereas navigational learning was performed in female WT and APP/PS1 (Figures 2, S10C, and S10D), as well as in male 5xFAD (Figures S10E and S10G), mice. Sequencing (Figure 3) and electrophysiology (Figure 4) experiments were performed after navigational learning in female WT and APP/PS1 mice. Animals were housed in a 12 h light/dark cycle with water and food available *ad libitum*, habituated to the experimenter for 2–3 days prior to the experiments and randomly assigned to experimental groups. Dox (0.2 mg/mL) was provided through the drinking water at least 7 days before surgeries and only ceased 2 days before the opening of the labelling window for engram tagging, after which it was immediately reintroduced.

METHOD DETAILS

Cloning, viral constructs and stereotaxic injections

The TRE::OSK construct was generated from pHAGE2-TetOminiCMV-OSK (a gift from Hans Schöler, addgene plasmid #136552[73]) subcloned into a modified pAAV backbone that includes a short expression cassette CW3SL (gift from Bong-Kiun Kaang, addgene plasmid #61463[74]), to ensure an appropriate size for AAV packaging. Viral particles were generated in house (EPFL's Bertarelli Foundation Gene Therapy Platform) for the TRE::OSK and cFos::tTA (gift from William Wisden, addgene plasmid #66794[75]) in the AAV8 serotype at a titer of $2.5x10^{13}$ VG/mL and $2.8x10^{13}$ VG/mL respectively. AAV8–TRE::GFP viruses were provided by UNC Vector Core, at a titer of $4.1x10^{12}$ VG/mL.

For surgeries, mice were anesthetized with an intraperitoneal mix of fentanyl (0.05 mg/kg) midazolam (5 mg/kg), and metedomidin (0.5 mg/kg) followed by fur shaving and subcutaneous injection above the head of an analgesic mix including lidocaine (6 mg/kg) and bupivacaine (2.5 mg/kg). Mice were then placed in the stereotaxic frame (Kopf Instruments), and their skin was disinfected and opened. Once the skull was cleaned and its orientation adjusted, holes were drilled at the desired positions according to the injection area. Viruses were injected bilaterally through pulled micropipettes (Blaubrand, intraMARK, 708707) at a rate of 0.2 μl/min in the following coordinates and volumes: DG, AP -1.9 mm, ML ± 1.3 mm, DV -2.0 mm; 300 nl per side; mPFC, AP +2.0 mm, ML ± 0.35 mm, DV 2.25 mm; 250 nl per side. Needles were left at the injection site for 5 min and then slowly pulled up to prevent backflow. After suturing the wound, mice were given atipamezole (2.5 mg/kg) to reverse anesthesia and placed in a heated cage with painkiller in the drinking water (Dafalgan 2 mg/ml) for recovery. Behavioral experiments started no sooner than 2 weeks after surgeries, and mis-injected animals, defined as those with poor transduction efficiency (<2% positive cells) or clearly mistargeted, were excluded from further analyses.

Fear conditioning

Fear conditioning was performed using a Multi Conditioning System (TSE) as previously described.[76] Briefly, on the day of conditioning, mice were acclimatized to the behavioral room for 30 min and then explored the conditioning box for 3 min. After this, mice received electric footshocks (2x0.6 mA or 3x0.8 mA, 2 s as indicated in the figures), and were moved to a holding cage 15 s later.

Please cite this article in press as: Berdugo-Vega et al., Cognitive rejuvenation through partial reprogramming of engram cells, Neuron (2025), https://doi.org/10.1016/j.neuron.2025.11.028

Recall occurred 2 days or 2 weeks afterwards (recent or remote, respectively), by exposing mice to the same conditioned context for 3 min without shocks. Freezing was used as a proxy for fear memory and quantified automatically by infrared beam cutting detection and using 1 s of immobility as threshold.

Water maze

Navigational experiments were performed using a Morris water maze as previously described.[77] Briefly, the maze consisted of a round pool of 165 cm diameter filled with opaque white water and containing an invisible platform (12 cm diameter, 2 cm from the surface). Sessions were recorded and tracked using Ethovision System (Noldus). The dropping position was shifted every day for a total of 3 days (6 trials per day) or 5 days (4 trials per day), as indicated in the figures. At the end of each trial (2 min) mice were gently guided to the top of the platform and then placed in holding cages under warm light. Swimming metrics and trajectories during the learning phase were analyzed automatically using Rtrack.[78] For the analysis of swimming strategies, one predominant strategy was assigned to every trial, including among spatial (hippocampal-dependent) and non-spatial (non-hippocampal) strategies. For navigational precision analysis, comparisons on the contribution between hippocampal and spatially precise- (*corrected* and *direct path*) vs imprecise- (*directed search*) scored trials, or metrics within them, were performed. Probe tests consisted of a single trial of 1 min duration without platform in which quadrant occupancy was evaluated (Ethovision software). For the reprogramming of spatial engrams in mPFC experiments (3-day protocol), Dox was removed after the first learning day in order to direct the window of engram labelling and reprogramming towards the third and last learning day, and re-introduced in the diet until the end of the experiment. For the tagging of engrams different from those involved in spatial learning, Dox was removed 2 days before exploration of a novel environment prior to water maze training. Briefly, animals were left to freely-explore a novel 40x40 cm box in a room adjacent to the water maze room for 15 min, after which Dox was immediately re-introduced and the water maze paradigm started 5 days later. Finally, for DG-targeting experiments aimed at studying changes during the learning phase itself, Dox was removed 2 days before the beginning of the protocol and learning extended for 5 days.

Ex vivo electrophysiology

GFP-injected WT and APP/PS1 mice and OSK-injected APP/PS1 were used for *ex vivo* electrophysiology two weeks after the 3-day-long water maze learning paradigm. Animals were anaesthetized with isoflurane and decapitated, and the brain was quickly removed and placed in oxygenated (95% O_2 / 5% CO_2) ice-cold N-Methyl-D-glucamine (NMDG)-based medium,[79] containing (in mM): 110 NMDG, 2.5 KCl, 1.2 NaH_2PO_4, 30 $NaHCO_3$, 20 HEPES, 10 $MgCl_2$, 0.5 $CaCl_2$, 25 glucose, 5 L(+)-ascorbic acid, 2 thiourea, 3 Na-pyruvate (titrated to pH 7.2-7.3 with HCl). Acute coronal slices containing the mPFC (250 μm thick) were cut using a vibrating tissue slicer (Campden Instruments). After cutting, slices recovered for 1 h at 35°C and subsequently at room temperature in a storage solution containing (in mM): 92 NaCl, 2.5 KCl, 1.2 NaH_2PO_4, 30 $NaHCO_3$, 20 HEPES, 2 $MgCl_2$, 2 $CaCl_2$, 25 glucose, 5 L(+)-ascorbic acid, 2 thiourea, 3 Na-pyruvate (titrated to pH 7.2-7.3 with NaOH). In the recording chamber, slices were superfused with oxygenated standard artificial cerebrospinal fluid (aCSF) containing (in mM): 130 NaCl, 25 $NaHCO_3$, 2.5 KCl, 1.25 NaH_2PO_4, 1.2 $MgCl_2$, 2 $CaCl_2$, 18 glucose, 1.7 L(+)-ascorbic acid.

Whole-cell patch clamp recordings were performed in visually identified GFP-positive neurons at nearly physiological temperature (30-32°C), with borosilicate pipettes (3-4 MΩ) filled with (in mM): 130 Kgluconate, 10 KCl, 10 HEPES, 10 phosphocreatine, 0.2 EGTA, 4 Mg-ATP, 0.2 Na-GTP, 0.1% biocytin (290-300 mOsm, pH 7.2-7.3). Current-clamp recordings were conducted using bridge compensation. To elicit neuronal firing, cells were held at -60 mV with direct current injections, and somatic current injections of increasing amplitude were provided using ramps of 5 s (6 ramps with final amplitude ranging from 50 pA to 300 pA). Input resistance (R_i) and cell capacitance (C_m) were assessed by the passive current response to a -10 mV hyperpolarizing step while cells were held at -60 mV. Resting membrane potential (V_{rmp}) and neuronal firing were measured within the first 5 min from the establishment of the whole-cell condition. The rheobase and the firing threshold were measured as the level of current and voltage, respectively, that induced the first action potential in the ramp protocol. The Kir3.1 channel activator ML-297 (AB143564) was dissolved in 50% DMSO/ 50% aCSF to 5 mM and perfused at a final concentration of 10 μM.[54,64] The effect of membrane potential was assessed by measuring mean voltage values in 1 min periods prior to and > 8m min after perfusion of the compound.

Signals were acquired through a Digidata1550A digitizer, amplified through a Multiclamp 700B amplifier, sampled at 20 kHz and filtered at 10 kHz for whole-cell recordings, or sampled at 4 kHz and filtered at 1 kHz for field recordings, using Clampex10 (Molecular Devices).

At the end of the recording, the patch pipette was carefully withdrawn from the cell body to facilitate membrane resealing. Brain slices were then fixed in 4% PFA overnight at 4°C, followed by transfer to a 30% sucrose solution in PBS. Thereafter, slices were washed three times for 5 min in PBS before being processed for immunofluorescence as detailed below, using the Klf4 primary antibody for identification of reprogrammed cells and streptavidin Alexa 647 (1:500, Thermo Fisher Scientific, S-32357) during secondary antibody incubation for identification of patched neurons. The final datasets comprise pyramidal neurons with confirmed localization in the deeper layers of the prelimbic cortex

Principal-component analysis and cognitive clock

Output files from Rtrack for every single water maze experiment were loaded in Python and further filtered for relevant spatial metrics (numerical with no missing value). Next, values for every metric were averaged over all trials resulting in one value per metric and per

Please cite this article in press as: Berdugo-Vega et al., Cognitive rejuvenation through partial reprogramming of engram cells, Neuron (2025), https://doi.org/10.1016/j.neuron.2025.11.028

mouse. Every metric was individually standardized by subtracting the mean and dividing by the standard deviation of each metric across individuals. Finally, a principal component analysis (PCA) model with two principal components was fitted using the scikit-learn python library and individual animals plotted in the two-dimensional space. Centroids were calculated as the averaged value per group of the first and second principal components. Euclidean distances to the centroid of young mice were calculated for GFP- and OSK-injected centroids, and these were compared by one-tailed paired *t* test.

To generate the cognitive clock, different regression models were trained to find the best predictor of age from spatial metrics, including ordinary least squares, ordinary least squares adjusted for multicollinearity and elastic net. Briefly, the training data consisted of a combination of relevant spatial metrics extracted from Rtrack for GFP-injected mice from 2 to 20 months old of age, which were assumed to reflect physiological age-related changes in learning. These metrics included: Median distance from goal, efficiency, goal crossings, initial trajectory error, path length, roaming entropy and velocity (see Rtrack documentation for a detailed explanation of each metric). Importantly, velocity was included among the relevant parameters used by the clock because differences in swimming speed exist between young, old and AD mice that help predict age from performance. However, velocity was not one of the parameters affected by OSK (Figure S10J). To select the most appropriate model, we allocated 30% of the training data to a test set and trained each of the three models with all of the remaining training set. Performance of the different models was assessed by R^2 value as well as mean squared error (MSE) on the training and test sets. The best performing model was the ordinary least squared adjusted for multicollinearity (Training MSE 19.365, Training R^2: 0.452. Test MSE: 22.686), in which highly correlated variables were removed based on their variance inflation factor value (VIF, >5 used as exclusion criteria). Once chosen, the whole training dataset was used to fit the final model in order to increase prediction accuracy.

Histology

Ninety minutes after the last recall session mice were administered a lethal dose of pentobarbital (150 mg/kg) and transcardially perfused with PBS followed by 4% paraformaldehyde (PFA) in PBS. Extracted brains were further fixed by overnight immersion in PFA, cryoprotected in 30% sucrose in PBS and stored at –80°C. Brains were cut at 30 μm in a cryostat and sections serially collected and preserved in antifreezing solution (30% ethylene glycol, 15% sucrose, 0.02% azide in PBS) until staining. For stereological quantifications using immunofluorescence one every six sections per brain area (for total of 6-10 sections) were used. Briefly, sections were first blocked and permeabilized in blocking solution (1% BSA, 0.3% Triton X-100 in PBS) for 2 h and then incubated with primary antibodies overnight at 4°C. The primary antibodies used were goat anti-GFP (AB6673, 1:1000), rabbit anti-GFP (AB290, 1:1000), mouse anti-GFP (AB1218, 1:1000), goat anti-Klf4 (AF3158, 1:400), guinea-pig anti-cFos (Sysy 226308, 1:4000), rabbit anti-Prox1 (AB101851, 1:1000), rabbit anti-H3K9me3 (AB176916, 1:500), rabbit anti-LaminB1 (AB229025, 1:1000), rat anti-Ctip2 (AB18465, 1:400). The following day, sections were washed three times in PBS and then incubated with secondary antibody (Invitrogen or Jackson Immunoresearch, 1:800) in blocking solution for 3 h. Finally, sections were washed in PBS, counterstained with DAPI (1:5000 in PBS, Invitrogen H3570) and washed three more times before mounting on glass slides and covered with Fluoromount-G medium to preserve fluorescence. For antibodies requiring antigen retrieval (H3K9me3 and Ctip2), sections were first mounted and dried on glass slides overnight. The day after, slides were rehydrated in PBS, submerged in 10mM citrate buffer pH = 6 and heated to 95°C for 20 min. After cooling in PBS, the normal staining protocol was performed on the slide, using a wet chamber. RNA scope was performed by the EPFL Histology Core Facility using the RNA Scope Multiplex Fluorescent V2 kit (ACD Bio) according to manufacturer's instructions. Briefly, Mm Pou5f1-O2 (Bio-techne, 1247361-C1), Mm Klf4-O1 (Bio-Techne, 813851-C2) and Mm Sox2-O1 (Bio-Techne, 1247371-C3) probes were hybridized simultaneously at 40°C for 2 h and signal was revealed with TSA Opal520 (Akoya Biosciences, FP1487001KT), 570 (FP1488001KT) and 650 (FP1496001KT) diluted 1:1500. Slides were next processed for additional antibody immunofluorescence as explained above.

Nuclei preparation for 10x multi-omics

For multi-omics, mice were sacrificed one day after the remote recall session of the water maze and the mPFC microdissected, flash-frozen in dry ice and finally stored in –80°C until processing. Nuclei were extracted as previously described.[80] Briefly, tissue of individual animals was kept on ice throughout the protocol and first homogenized in 600 μl of homogenization buffer (250 mM sucrose, 25 mM KCl, 5 mM MgCl2, 10 mM Tris·HCl, pH 7.4, 1 mM DTT, 1X protease inhibitor, 1 U/μl RiboLock RNAse inhibitor, 0.1% NP-40, in H_2O), gently filtered through a 40 μm cell strainer and washed with 1500 μl nuclei isolation medium (without NP-40). Samples were centrifuged for 8 min at 1000g and pellet resuspended in 210 μl of isolation medium and then added 290 μl of 50% iodixanol (optiprep, IDM 1X, 1 mM DTT, 1X protease inhibitor 50X, 1 U/μl RiboLock RNAse inhibitor). Nuclei suspension was carefully transferred to a Beckman tube (ref: 344090) and completed with 100 μl of nuclei isolation medium layered on top before ultracentrifugation at 10000g for 22 min using a SW 55 Ti rotor, for debris separation. The nuclei pellet was resuspended in 100 μl of permeabilization buffer (nuclei isolation medium plus 0.01% Tween, 0.001% digitonin, 0.01% NP-40, 0.5% BSA), kept on ice for 2 min at 4°C and finally washed in 500 μl of nuclei isolation buffer plus 0.5% BSA. Samples were centrifuged at 1000g for 10 min at 4°C, pellets resuspended in diluted nuclei buffer (Chromium nuclei isolation kit, 10X Genomics) and nuclei filtered through a 40 μm Flowmi strainer before counting (average yield of 4000 nuclei/μl). Finally, nuclei were processed for Chromium Next GEM Single Cell Multiome ATAC + Gene Expression sequencing by the Gene Expression Core Facility (EPFL). One library was generated for each brain sample. Samples from all groups were processed in two different batches. In each batch, all libraries were pooled and sequenced on NovaSeq 6000 to an average depth of ~40000 reads per cell.

Please cite this article in press as: Berdugo-Vega et al., Cognitive rejuvenation through partial reprogramming of engram cells, Neuron (2025), https://doi.org/10.1016/j.neuron.2025.11.028

QUANTIFICATION AND STATISTICAL ANALYSIS

Imaging and quantifications

For cellular quantifications, images from at least 3 sections per animal were acquired using an Olympus SlideScanner VS120 L100 with 10x (for mPFC, 0.65 μm pixel size) or 20x (for DG, 0.32 μm pixel size) objectives. Quantifications in DG experiments was restricted to the dorsal DG (from Bregma –1.5 to –2.5 mm; Figure S1J), whereas mPFC quantifications were restricted to the anterior cingulate, prelimbic and infralimbic regions of the mPFC, rostral to the callosal junction (from Bregma 2.25 to 1.45mm; Figure S3J). Cell numbers for engram reactivation analyses were extracted using QuPath automatic cell detection and co-localizations scripts. Briefly, cells positive for individual channels (e.g., GFP^+, $Klf4^+$, $cFos^+$) were first detected according to manually pre-set thresholds relative to the background noise and later classified as double or triple positive by proximity. Total numbers of cells were estimated via detection of $DAPI^+$ cells, which was then used to calculate densities and chance probabilities.

For cellular intensity measurements, images from at least 3 different sections per animal were acquired using a Upright Leica DM6 CS confocal microscope for protein immunofluorescence (40x immersion objective at 221.95 nm pixel size) or a Zeiss LSM980 inverted confocal microscope for RNAscope (40x at 82 nm pixel size or 63x at 71 nm pixel size for mPFC and DG, respectively). Scanning was performed sequentially to prevent bleed-through signal between channels, and tilescans of the interest areas were stitched using Leica LAS-X software. In the event of poor antibody penetration or irregular signal at the selected confocal plane, images were acquired as z-stacks (1.1 μm step size) and then projected on the focal point with most regular signal using the LocalZprojection plugin in Fiji. Final images for intensity quantifications were analyzed using QuPath.[72] First, nuclei were detected using the StarDist plugin set to the acquired pixel size and measurements per cell including signal intensities and circularities were exported and finally filtered and analyzed using custom R scripts (v. 4.3.2). Only nuclei bigger than 35 μm^2 were used for quantifications. When needed, nuclei were additionally classified as positive or negative for the specific channel (e.g., GFP^+, $Klf4^+$ or $probe^+$) according to a manually pre-set threshold.

Raw cell intensity signals (for intra-section comparisons) or normalized by DAPI (for inter-animal comparisons) were used. In the case of LaminB1, only the signal ranging from the nuclear membrane to 5 pixels inwards was quantified. For intensity classification, raw intensities of all cells per animal were transformed to z-scores [(observed cell signal – mean signal of all cells) / standard deviation of all cells] and divided using the third and first quartile in high, medium and low expressing cells, among which percentages of positive and negative cells (Klf4, GFP or probe) were calculated. Data is expressed per cell or per animal, as indicated.

Statistics and reproducibility

Quantification of cell numbers and intensity analyses were performed on independent biological replicates (N = mice and n = cells counted per mouse) and depicted as medians, means ± SDs, ratios or log-transformation of ratios for data linearization, box–whisker and violin plots, as indicated in the figure legends. Statistical analyses were performed in Prism 10 (GraphPad) and significance was assessed by two-tailed, unpaired (different animals) or paired (same animal or group) Student's t test and ANOVA (one or 2-way) or non-parametric version. Behavioral analyses were performed on 7–15 mice per group (as indicated in figure legends) from at least 2 different batches. Data is depicted as area or bar charts (navigational strategies), bar graphs (freezing), means ± SEM (path length and velocity) and box-whiskers plots (probe tests). Statistical significance was calculated by Wald test of odds ratios assessed by logistic regression (navigational strategies), one-way (freezing and quadrant occupancy) or repeated measures 2-way (path length, velocity) ANOVA. Electrophysiological analyses were performed on N = 5 mice per group. Data are depicted as means ± SEM for firing frequencies and as bar graphs with average per patched cell. Statistical significance was calculated by ANOVA (one or 2-way) or non-parametric version. Table S7 includes the statistical test and significance of all cellular, behavioral and electrophysiological analyses in the manuscript. Statistics used in the multiome analyses are detailed in their respective sections below.

10X data processing and quality control

Single-nucleus RNA and single-nucleus ATAC sequencing (snRNA-seq and snATAC-seq) libraries were processed with CellRanger-arc software (v. 2.0.0) using a custom mouse reference genome built from the mm10 genome and combined with the injected viral constructs for identification of infected GFP^+ and OSK^+ cells.

Downstream analysis was performed using custom R scripts. To create a multiomic Seurat object with paired gene expression and DNA accessibility profiles for each sample, Seurat (v 5.0.3)[81] and Signac (v. 1.13.0)[82] pipelines were followed with the default settings unless specified. For chromatin accessibility, MACS2[83] was used to call peaks from the fragment files. Peaks on nonstandard chromosomes overlapping annotated genomic blacklist regions from the mm10 genome were removed. Fragment counts for each peak per cell were then quantified using the FeatureMatrix function in Signac. Per-cell quality control metrics for each modality were computed, including mitochondrial percentage, nucleosome signal, TSS enrichment score and percentage of reads in peaks. Next, the individual Seurat objects from each sample were combined into one single object using the merge function in Seurat.

For gene expression downstream analyses, quality control filtering was done by retaining cells with total RNA-seq count >500 and <30000, features detected >200 and <9000 and mitochondrial percentage <2%. A total of 34,603 cells were kept for snRNA-seq. Gene expression values [E (I, j)] for gene I in cell j were then calculated by dividing UMI counts for gene I by the sum of the UMI counts in nucleus j, to normalize for differences in coverage, and then multiplying by 10,000 to create TP10K (transcript per 10000) values,

Please cite this article in press as: Berdugo-Vega et al., Cognitive rejuvenation through partial reprogramming of engram cells, Neuron (2025), https://doi.org/10.1016/j.neuron.2025.11.028

and finally computing $\log_2$(TP10K + 1) using the NormalizeData function from Seurat. The normalized data was scaled using the ScaleData function from Seurat, yielding the relative expression of each gene by scaling and centering.

For chromatin accessibility, additional quality control filters were applied, retaining cells with total ATAC-seq count >1000 and <75000, nucleosome signal <2, TSS enrichment score >3 and a fraction of peaks mapping to blacklisted regions <0.1. Peaks that were detected in <10 cells were removed. A total of 32,150 cells were kept for snATAC-seq. ATAC-seq peaks were then normalized using the log-TF version of the term frequency–inverse document frequency (TF-IDF) transformation by using the RunTFIDF function in Signac (parameter setting: "method = 3").

Dimensionality reduction and cell type identification

The scaled gene expression matrix restricted to the top 1000 variable genes was used for PCA, using the RunPCA method in Seurat (a wrapper for the irlba function), computing the top 35 principal components. Scores from these principal components were used as the input to downstream clustering and visualization by Uniform Manifold Approximation and Projection (UMAP). Clustering was performed using the Seurat functions FindNeighbors and FindClusters (resolution = 0.4). No batch effects were observed in the UMAP visualization of the gene expression data. Cell types were annotated in an unsupervised manner by the SingleR package[84] using the Allen Brain Atlas whole cortex and hippocampus dataset[37] and using the Wilcoxon ranked sum test to identify the top markers for each pairwise comparison between labels (see Table S2 for excitatory neuron markers). Cell type identities were confirmed by visual inspection of the top marker genes of each cluster obtained using the FindAllMarkers function from Seurat. Two clusters were manually annotated: Disease Associated Microglia (DAM), which shows a clear enrichment for DAM markers[85–87] and oligodendrocyte precursors, which shows a high expression of *Pdgfra* gene, a marker of this cell type.[88] Additionally, cells with at least one RNA-seq read mapping to either of the TRE::GFP or OSK viral constructs were labelled as engram cells. Cell type and engram identifications were used both for gene expression and chromatin accessibility downstream analyses

For ATAC-seq, the top 25% most frequently observed peaks of the TF-IDF matrix were then selected by the FindTopFeatures function for singular value decomposition using the RunSVD function in Signac. The 2:20 first LSI components were used for batch correction using Harmony[89] and for visualization in UMAP.

Cellular proportion analysis

To gain insight into cell type alterations, the relative proportion of the number of nuclei in each cell type was normalized to the total number of nuclei captured from each library. To determine if any changes in cell-type proportion were statistically significant, single-cell differential composition analysis (scDC)[90] was implemented to bootstrap proportion estimates for our samples. We employed a linear mixed model (random effect of subject) to determine if any changes in cell-type proportion were present.

Differential expression analysis

All clusters identified as belonging to the same major cell type (excitatory neurons, interneurons and non-neurons) were merged for differential gene expression analyses. Within each cell type, WT and APP/PS1 and APP/PS1 OSK samples were compared for differential gene expression using the logistic regression framework implemented in Seurat's FindMarkers function to minimize false positives.[91] Batch and count number of each cell were added as latent variables in the analysis. Only genes expressed in at least 10% of the cells from one of the groups for that cell type were included in the analysis. After correcting for multiple testing, only genes with a p adjusted value < 0.05 and an absolute $\log_2$ fold-change greater or equal to 0.1 were considered for downstream analyses. The significance of the overlap of differentially expressed genes between comparisons was tested using the GeneOverlap R package, setting the genome.size to the number of genes detected in the cell type of interest. Table S1 contains all differentially expressed genes.

Generation of identity, engram and AD engram scores

The identity score was calculated by computing the Spearman correlation value for SingleR-identified cell-type-specific markers between each cell and the reference Allen Brain Atlas dataset. For the generation of the engram score, we first identified genes relevant for engram formation upon differential expression analysis of engram vs. non engram cells of WT mice (WT engram signature). Similarly, for the generation of the AD engram score, we identified genes differentially expressed in AD engrams from the analysis of APP/PS1 vs. WT engram cells (AD engram signature). These genes were then used to infer the engram and AD engram pseudotimes of WT, APP/PS1 and OSK engram cells using the Monocle 2 package.[92] The pseudotime score of each cell was used as its engram and AD engram scores. Table S2 contains all the genes used for the generation of each score.

Gene Ontology and gene set enrichment analysis

Differential expression signatures were tested for enriched Gene Ontology processes, using a hypergeometric test (shinyGO, v0.80),[93] and corrected for multiple hypotheses by false discovery rate (FDR). Biological processes with p adjusted value < 0.05 were reported as significantly enriched. The list of genes detected in each cell type was used as the universe for the hypergeometric test of each comparison. Table S3 contains all significant GO processes identified in the different comparisons. Additionally, to identify pathways that change in APP/PS1 and OSK-mediated reprogramming, the gene list obtained by logistic regression was ranked by decreasing $\log_2$FC score, and then pathway enrichment was performed using the GSEA algorithm implemented in

Please cite this article in press as: Berdugo-Vega et al., Cognitive rejuvenation through partial reprogramming of engram cells, Neuron (2025), https://doi.org/10.1016/j.neuron.2025.11.028

the Genekitr R package, and GO mouse pathways limited to the "Biological Process" category. Table S4 contains the output of the GSEA analysis.

Differential accessibility analysis

Following cell type annotation, a new set of peaks was called grouping cells by cell type and group. Peaks were annotated with annotatePeak from the R package ChIPseeker (v1.38.0),[94] using the library TxDb.Mmusculus.UCSC.mm10.knownGene. For each cell type, WT and APP/PS1 and APP/PS1 OSK samples were compared for differential chromatin accessibility using the logistic regression framework implemented in Seurat's FindMarkers function. Batch and fragment number were added as latent variables in the analysis. Only peaks present in at least 5% of the cells from one of the groups for that cell type were included in the analysis. Peaks with a p value < 0.001 and an absolute log fold-change > 0.25 were considered as significant. Table S5 contains all differentially accessible regions.

Transcription factor motif enrichment, activity and footprint analysis

For each comparison, significant peaks were tested for overrepresentation of each DNA motif from the JASPAR 2020 database[95] by using the FindMotifs function in Signac. The resulting p values were FDR adjusted. To investigate transcription factor enrichment among downregulated genes upon OSK reprogramming, the ChEA3 API platform was used with default settings, and ChEA3 score calculated as the inverse of the ChEA mean rank. Table S6 contains all ChEA3-identified transcription factors. The per-cell motif activities were inferred using the Signac wrapper for chromVAR,[96] which identifies motifs associated with variability in chromatin accessibility between cells. The differences in motif activity between groups were tested using the logistic regression framework implemented in Seurat's FindMarkers function, including batch as a latent variable. To compute and plot the footprint of each factor, a complementary readout of transcription factor activity, the Footprint and PlotFootprint Signac functions were used.

Gene expression - chromatin accessibility correlation

To investigate how chromatin accessibility changes influenced gene expression in the dataset, $\log_2$FC of significant DEGs were correlated to $\log_2$FC of promoter or linked peaks. For gene-promoter associations, only peaks located by ChIPseeker in the promoters of the DEGs were included in the analysis. Linked peaks were determined using Signac's LinkPeaks function with a 150 kb window for a gene's TSS. For both comparisons, the $\log_2$FC of all associated peaks were averaged and used to calculate the Pearson correlations using cor.test in R.

Coverage plots were generated using the Signac function CoveragePlot, which displays linked peaks and normalized ATAC signals obtained by calculating the averaged frequency of sequenced DNA fragments for the different groups of cells.